Delft University of Technology

Master Thesis

A Comparison of Dutch Atmospheric Large-Eddy Simulation (DALES) of Atmospheric Flow over Hills with Bolund Experiment

Author:

Bart Warmerdam

Thesis committee

Dr. S.R. de Roode

Prof. dr. A. P. Siebesma

Prof. dr. ir. C. Kleijn

August 25, 2021

Abstract

The Dutch Atmospheric Large-Eddy Simulation (DALES) model is a computational model to study the flow in the atmospheric boundary layer (ABL). The present study critically tests a module that has been developed for DALES to simulate buildings and hills in the ABL, called the Immersed Boundary Method (IBM). The analysis is done under neutral atmospheric conditions, which entails that heat and moist fluxes do not play a role in the wind development. Only the velocity shearing affects the wind profiles. The performance of DALES in this Neutral Boundary Layer (NBL) is first tested with a flat surface. The NBL simulation by DALES shows that DALES can approximate the surface layer turbulence structure well and that convergence is established for grid sizes smaller than $\Delta x = \Delta z = 4$m. Only in the grids directly above the surface is the wind profile, as quantified by the dimensionless wind shear Φ_M and the subfilter-scale turbulent kinetic energy (SFS TKE) overestimated because the SFS fluxes that dominate, excessively produce TKE. In the upper part of the ABL it is found that the domain width in DALES is the key variable for converging results. The IBM module is validated by comparing the DALES-IBM simulation with Bolund hill observations. The simulated wind above the Bolund hill by DALES-IBM is approximating the front and ridge velocity profiles well. The simulated TKE had the correct characteristics as observations as well although the average error was higher than the average velocity error. The modelling of the wake of Bolund is the point of interest. The simulation showed hardly any velocity and TKE in the wake, while the TKE should be high. The expected reason lies within the shear calculations of the IBM. These calculations are based on lower Reynolds numbers and calculate too little shear. The simulated velocity profiles converged, thus the discretisation errors of IBM are limited. The next steps for IBM are to change the shear calculations and validate the heat and temperature dynamics.

Contents

1   Introduction

1.1   Dutch Atmospheric Large-Eddy Simulation

The research concerning atmospheric weather forecasting heavily depends on computational numerical models. Common computational models are the Large-Eddy Simulation (LES), Reynold-Averaged Navier Stokes (RANS) and Direct Numerical Simulation (DNS). The principe behind LES modeling is a spatial filter such that most turbulence is resolved (Wyngaard 2004). The smaller, less energetic scales are parameterized. DNS resolves all length scales and RANS uses a temporal filter. LES is especially used for domains between 1 and 3000 kilometer, which is too large for DNS, while the turbulence model of LES is normally better suited for these length scales than RANS (Travin et al. 2004).
LES is for this reason widely used for modelling the Atmospheric Boundary Layer (ABL). The ABL is part of the troposphere and it is the region of the atmosphere which is directly influenced by the surface. It is typically one kilometer high. The rest of the troposphere is called the free atmosphere. The ABL is influenced by diurnal cycles and turbulence due to surface forcing, while the free atmosphere shows little variation over timescales of a day and smaller (Stull 1988).

The development of LES models started in the late sixties. The LES models improved as research grew and computation costs declined. A recent improvement of LES is the module to use non-flat surfaces. Earlier LES models used flat surfaces. However, relief often distorts the weather far away from the hills itself (De Wekker and Kossmann 2015). Even hills in the Netherlands influence the weather.
The Dutch Atmospheric Large-Eddy Simulation model (DALES) is the LES version widely used in Dutch academics (Heus et al. 2010). The first application for DALES that used non-flat surfaces was a simulation of wind and pollution around cities, where streets and buildings needed to be distinguished. The possibility for buildings to be modelled is developed and described by Tomas (2016) and further developed by Koene (2020). The method used is called the Immersed Boundary Method (IBM). It models buildings as impenetrable blocks by not allowing velocity, heat and scalar fluxes through. This technique is not limited to cities and could potentially suffice as method to implement hills in DALES. Hills are then modelled as impenetrable blocks on top of the surface.

1.2   Bolund hill

The potential of DALES-IBM for hills is yet unclear. DALES itself has been validated (Heus et al. 2010), but the IBM module is not. There are a couple of sites where an extensive amount of wind velocity data has been gathered on hilly terrain, most notably the Askervein hill in the United Kingdom (Taylor and Teunissen 1987) and the Bolund hill in Denmark (Berg et al. 2011). Both hills could be used as a

comparison case to validate DALES-IBM. The Askervein hill is smoothly increasing with few sections over 20° and various models have proven to be able to model the hill appropriately, see for instance Castro et al. (2003) (RANS) and Lopes et al. (2007) (LES). The Bolund site is steeper and more complex. It gives rise to recirculation and it is therefore a more comprehensive validation case. There has already been an extensive study on the Bolund hill between various models, in which LES models did poorly (Bechmann et al. 2011), and worse than RANS. This was however an anonymous test and none of the LES models used the Immersed Boundary Method. This report is the second validation for LES-IBM for wind flow around complex hills, whereas the first (Diebold et al. 2013) used a different stress calculation.

All Bolund hill data and information can be found in Berg et al. (2011) and Bechmann et al. (2011). The Bolund hill is an island that lies in Denmark (latitude $\phi = 55.7°$) and is therefore part of the mid-latitudes like the Netherlands. It is at most 12 meters tall and its size is 130 (West-Earth) by 75 meters (North-South). The Bolund hill is therefore smaller than mesa hills (120-360m high), which can be found in Limburg, and Gelderland in The Netherlands. The validation of DALES-IBM must therefore not be seen as direct validation for these scales, but as stepping stone.

The surface layer is the lowest part of the ABL and its height is typically under 100 meters (Kent et al. 2018), which includes the Bolund hill and the wind masts. The surface layer is therefore the important ABL layer in this report.
The Bolund hill data is retrieved under neutral boundary layer (NBL) conditions. The atmosphere is determined by velocity shearing forces in the NBL. The NBL is chosen for this reason, since possible other fluxes such as heat and water will not influence the results.

1.3   Thesis objectives

Three objectives are posed for this thesis:

- Study the turbulence structure as obtained from DALES in the NBL and compare the surface layer results to known theory.

- Find the large scale pressure that drives the flow in the Bolund hill experiment.

- Study the performance of DALES-IBM on the Bolund case. This performance is measured in terms of convergence of the model and in comparison to the Bolund data and participating models in (Bechmann et al. 2011).

1.4 Outline

This report is organised as follows. The general theory behind atmospheric flow and Large-Eddy Simulations is described in section 2. The Immersed Boundary Method as it is used in DALES is the topic of section 3. The description of the cases for both the flat runs as for the hill runs is given in section 4. The simulations of the flat NBL by DALES and its interpretation are presented in section 5. The simulations of the Bolund simulation and its interpretation are presented in section 6. The Bolund simulation results are discussed in section 7. The conclusion is drawn in section 8.

2 Modelling Atmospheric Flow

Atmospheric fluid flow is governed by conservation of mass, momentum, energy and water content. In this report water content will not be relevant and it will not be discussed. The remaining equations and the modelling thereof is the topic of this section. The governing equations will be discussed in section 2.1 and the modelling of these governing equations by Large-Eddy Simulations will be described in section 2.2. The grid and domain theory for LES is discussed in section 2.3.

2.1 Governing equations

The conservation of mass is described by equation 1. Although air is not incompressible, it will be modelled as such since density fluctuations are insignificant for mass conservation.

$$\frac{\partial u_i}{\partial x_i} = 0 \tag{1}$$

The Einstein notation is used: $i = 1, 2$ denote the horizontal directions x, y, and $i = 3$ denotes the vertical direction z. $(u_1, u_2, u_3) = (u, v, w)$ are the velocity components.

The momentum equation for fluids is the Navier-Stokes equation. The Navier-Stokes equation for Newtonian gases such as air reads

$$\frac{\partial u_i}{\partial t} + u_j \frac{\partial u_i}{\partial x_j} = -\frac{1}{\rho} \frac{\partial p}{\partial x_i} + \nu \frac{\partial^2 u_i}{\partial x_j^2} - g\delta_{i3} + \mathfrak{f}_i. \tag{2}$$

where t is the time, ρ is the density, p is the pressure, ν is the kinematic viscosity, $g = 9.81 \text{ms}^{-2}$ is the gravitational acceleration, δ_{mn} is the kronecker delta and $\mathfrak{f}_i$ consists of possible body forces. Equation 2 can be simplified for atmospheric flow. Atmospheric flows have high Reynolds numbers, $Re = \frac{UL}{\nu} >> \frac{1 \cdot 100}{1.4 \cdot 10^{-5}} >> 10^5$ such that the diffusion term $\nu \frac{\partial^2 u_i}{\partial x_j^2}$ becomes insignificant. The Coriolis force is present, since the Earth is a non-inertial reference frame.

$$\mathfrak{f}_{i,\text{cor}} = \epsilon_{ijk} u_j f_k \tag{3}$$

ϵ_{ijk} is the Levi-Civita symbol and $f_k = 2\Omega[0, -\cos(\phi), \sin(\phi)]$ is the Earth's angular velocity vector, with $\Omega = 7.3 \cdot 10^5 \text{rads}^{-1}$ the angular velocity of the Earth and ϕ the latitude. f_2 will become irrelevant in the Navier-Stokes equation for atmospheric flow, as can be deducted via scale analysis (Wyngaard 2010). f_3 will from now be called f. The advection term of the momentum equation 2 can be rewritten with aid of equation 1.

$$\frac{\partial u_i u_j}{\partial x_j} = u_j \frac{\partial u_i}{\partial u_j} + u_i \frac{\partial u_j}{\partial u_j} = u_j \frac{\partial u_i}{\partial u_j} + 0 \tag{4}$$

The Navier-Stokes equation then reads

$$\frac{\partial u_i}{\partial t} + \frac{\partial u_i u_j}{\partial x_j} = -\frac{1}{\rho} \frac{\partial p}{\partial x_i} - g\delta_{i3} + \epsilon_{ij3} u_j f \tag{5}$$

2.2 Large-Eddy Simulations

It is not possible to solve equation 5 analytically and it can only be solved numerically. One method to solve the numerics is LES. LES divides the domain in grid boxes distinguished per direction (i, j, k). Within the grid box a variable can be expressed in terms of a filtered mean value from scales larger than grid box size Δ and fluctuations with respect to this mean ϕ', which is called the subgrid contribution.

$$\phi = \widetilde{\phi} + \phi' \tag{6}$$

For LES to properly function, it is necessary that $\phi \approx \widetilde{\phi}$ and $\phi'/\widetilde{\phi} << 1$, because LES calculates $\widetilde{\phi}$. The filtering operator $\widetilde{\cdot}$ converts the incompressibility formula 1 into

$$\frac{\partial \widetilde{u}_i}{\partial x_i} = 0. \tag{7}$$

The Navier-Stokes equation can also be filtered. The elaborated version is shown in the Appendix. The result, along with the Boussinesq approximation for the density, reads

$$\frac{\partial \widetilde{u}_i}{\partial t} + \frac{\partial (\widetilde{u}_i \widetilde{u}_j)}{\partial x_j} = -\frac{1}{\rho}\frac{\partial p_\infty}{\partial x_i} - \frac{\partial \widetilde{\pi}}{\partial x_i} + g\frac{\widetilde{\theta} - \theta_0}{\theta_0}\partial_{i3} - \frac{\partial \tau_{ij}}{\partial x_j} + \epsilon_{ij3}\widetilde{u}_j f \tag{8}$$

(Heus et al. 2010), where p_∞ is the large scale pressure, $\pi = \frac{p-p_0}{\rho_0} + \frac{2}{3}\widetilde{e_{\text{sgs}}}$ is the modified pressure and θ is the potential temperature, which reads

$$\theta = T\left[\frac{p}{p_{\text{ref}}}\right]^{-R_d/c_p} \tag{9}$$

with p_{ref} the reference pressure set equal to 10^5Pa, $R_d = 287.04$Jkg^{-1}K^{-1} the gas constant for dry air and $c_p = 1.004$Jg^{-1}K^{-1} the specific heat of dry air.

The large scale pressure gradients are not solved within the domain, but prescribed. It is the most important input setting in DALES for this report. This is done via the geostrophic wind components U_{g} and V_{g}, whose definitions read

$$U_{\text{g}} \equiv -\frac{1}{f\rho}\frac{\partial p_\infty}{\partial y}$$
$$V_{\text{g}} \equiv +\frac{1}{f\rho}\frac{\partial p_\infty}{\partial x}. \tag{10}$$

Furthermore

$$\tau_{ij} = \widetilde{u_i u_j} - \widetilde{u}_i\widetilde{u}_j - \frac{2}{3}\delta_{ij}\widetilde{e_{\text{sgs}}} \tag{11}$$

where $\widetilde{e_{\text{sgs}}} = (\widetilde{u_i u_i} - \widetilde{u}_i\widetilde{u}_i)/2$ is the subgrid kinetic energy. The last equation to close the set of equations is the approximation of τ by

$$\tau_{ij} = -K_m\left(\frac{\partial \widetilde{u}_i}{\partial x_j} + \frac{\partial \widetilde{u}_j}{\partial x_i}\right) \tag{12}$$

where K_m is the eddy viscosity (Lesieur et al. 2005), which is

$$K_m = C_m \lambda \widetilde{e_{\text{sgs}}}^{1/2} \tag{13}$$

for DALES (de Roode et al. 2017) with $C_m = 0.12$ and λ a length scale dependent on the grid sizes. Fluxes of scalars ϕ are calculated by

$$\widetilde{u'_j \phi'} = -K_h \frac{\partial \widetilde{\phi}}{\partial x_j} \tag{14}$$

with $K_h = \text{Pr}_\text{T} K_m$, where Pr_T is the turbulent Prandtl number. All terms dependent on K_m or K_h are so called subgrid-terms. The subfilter-scale energy present in equation 13 needs to be computed. Its budget equation reads

$$\frac{\partial \widetilde{e_{\text{sgs}}}}{\partial t} + \widetilde{u}_j \frac{\partial \widetilde{e_{\text{sgs}}}}{\partial x_j} = \frac{g}{\theta_0} \widetilde{w'\theta'} - \widetilde{u'_i u'_j} \frac{\partial \widetilde{u}_i}{\partial x_j} + \frac{\partial}{\partial x_j} 2K_m \frac{\partial \widetilde{e_{\text{sgs}}}}{\partial x_j} - c_\epsilon \frac{\widetilde{e_{\text{sgs}}}^{3/2}}{\lambda} \tag{15}$$

with c_ϵ a proportionality constant. The derivation can be found in Lesieur et al. (2005) and de Roode et al. (2017). The tilde-operators are now omitted for the rest of the report for easy readability.

All variables are defined in the grid cell center, except for the velocity components. They are defined on the cell face facing the preceding grid cell. The velocity $u(i, j, k)$ is for example defined at $(i - 1/2, j, k)$. See figure 1. The DALES features are explained in Heus et al. (2010).
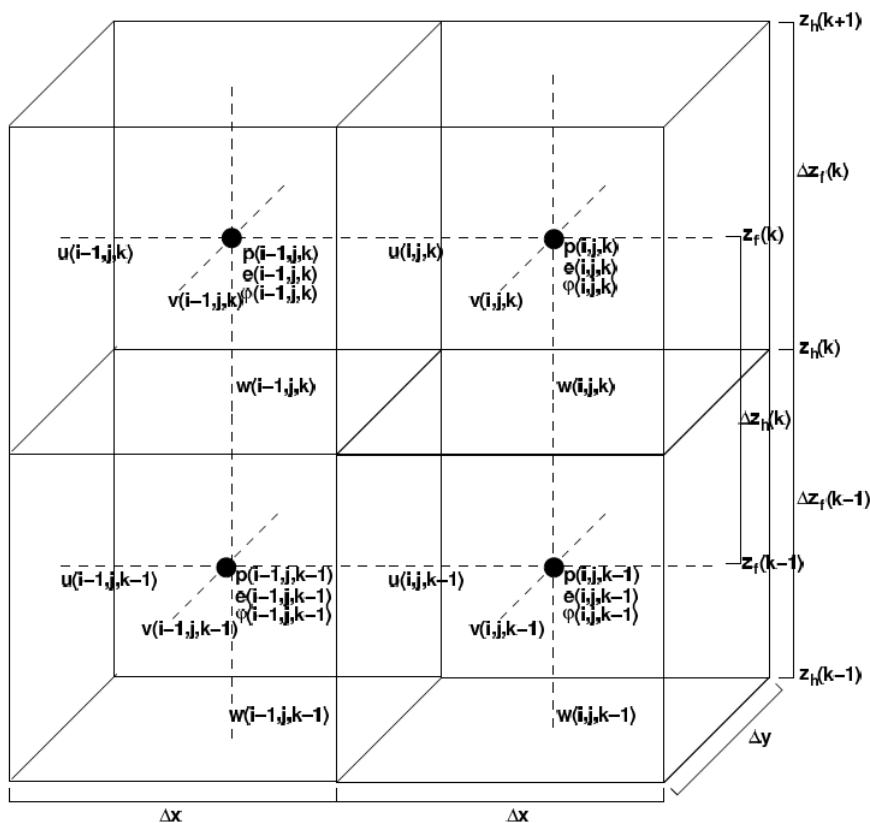
Figure 1: The grid used in DALES with the properties at their respective positions. Image taken from (Heus et al. 2010).

2.3 Grid and Domain Sensitivity

The determination of appropriate grid and domain sizes is an important process for LES simulations. The computational cost is proportional to the number of grid points in the horizontal directions N_x, N_y and the number of grid points in the vertical direction N_z. On the other hand, the results improve with finer horizontal grid lengths Δx, Δx and with a finer vertical grid height Δz. Larger domains also provide better results. Because of convenience it is selected that $\Delta x = \Delta y$, $N_x = N_y$ and $l_x = l_y$.

Grid Sensitivity

The appropriate grid sizes are the largest grid size where the mean statistics have approached the results of the smallest resolution (Beare et al. 2006). Numerous studies have been performed to assess the appropriate grid sizes, see for instance Dai et al. (2021). Beare et al. (2006) suggests that the grid size $\Delta = (\Delta x \Delta y \Delta z)^{1/3}$ should be $\Delta \leq 3.125$m and notes a 20 % error for $\Delta = 6.25$m in the Stable Boundary Layer case for an ABL height h of 250m. Sullivan and Patton (2011) advises $\frac{h}{\Delta} > 60$ for the Convective Boundary Layer case. This results in Δ to be 25 meter for

$h = 1500$m, a typical CBL height. The NBL has been studied by Ercolani et al. (2017) and they suggest $\Delta x = 16$m and $\Delta z = 4$m, for $h \approx 1000$m. However, this was their finest grid size and they did not reach a convergence.

Domain Sensitivity

LES models have to include the entire ABL plus a margin of about 30% in its vertical domain length l_z to correctly model any part of the ABL. It is not possible to only model the surface layer, because the upper boundary conditions of LES cannot cope with that.
The width of an LES run l_x has to be broad enough to capture all eddy sizes. The domain width must be selected appropriately.

3 Modelling hills with the Immersed Boundary Method

Large-Eddy Simulations use by default a Cartesian coordinate system with a flat surface, located below the lowest grid boxes. The effect of the surface on the air in terms of turbulent fluxes just above it is parameterised and dependent on the air properties in the lowest grid box and on the surface properties. Hills complicate the grid of LES and the surface forcings, because of the inherent heterogeneity of a hill. The IBM was developed recently by Tomas (2016) for DALES and this reports aims to validate his module. The module is described in section 3.1. Its greatest counterpart to model hills, the Terrain-Following Coordinates method, is shortly described in section 3.2.

3.1 Immersed Boundary Method

The immersed boundary method uses the same governing equations as an LES run of a flat surface, with appropriate boundary conditions to prevent flow into obstacles and to add wall friction effects. The flow in entire domain is first calculated as if there were no walls. After that, the effect of the wall is added. There are multiple methods to do so, read for example Diebold et al. (2013) and Bao et al. (2018). The method used in this research is called the wall function (Koene 2020). An immersed boundary must be loaded in DALES, with the immersed boundary representing the hill. The immersed boundary selects grid boxes to be hill, instead of air. A grid box is either fully air or fully hill. In figure 2 an example is shown of five dark grey grid boxes that will act as impenetrable and thus as immersed boundaries in their domain.
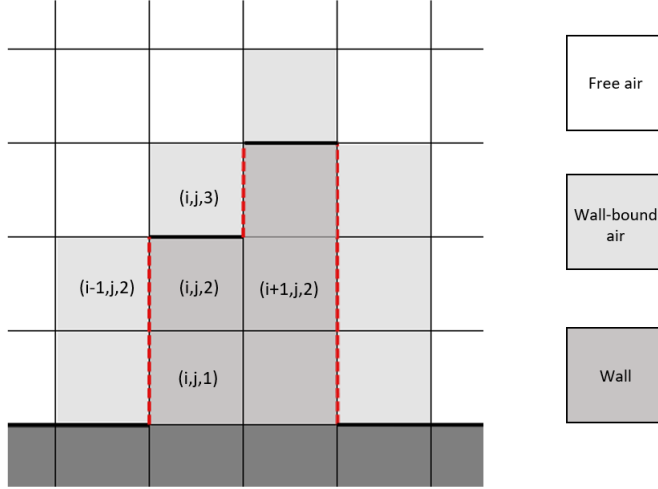
Figure 2: The three types of grid boxes important to IBM modelling. All grid boxes are indicated by their position (i, j, k). The immersed boundary grids are dark grey. Adjacent grid boxes to the walls, in light grey, are still influenced by the wall. The horizontal (black) walls act different than the vertical (red dashed) walls such that forcings in vertical wall-bound air grid boxes are different than forcings in horizontal wall-bound air grid boxes.

The IBM module distinguishes free air, wall-bound air and wall grid boxes. The IBM module adjusts nothing in the free air grid point. In the wall grid points, all forcings are set such that variables return to their ground surface value. The velocity then stays zero and the potential temperature stays at the potential temperature of the ground surface.

The grid boxes that are most extensive to model are the wall-bound air grid boxes, the light grey grid boxes in figure 2. These boxes can be split in bounded by a horizontal wall and bounded by a vertical wall, or by both. In case of both, both the horizontal and vertical wall forcings are applied.

3.1.1 Wall-bound grid boxes bound by horizontal walls

The horizontal walls act as if the surface is now on top of the immersed boundary. Its effect is that the parametrizations of the surface are now used on level $k_{\mathrm{IB}} + 1$, with k_{IB} the k value of the highest immersed boundary at the horizontal position (i, j). In the example of figure 2, this would be 2 for (i, j) and 3 for $(i + 1, j)$. The parametrization for the shear is calculated via the friction velocity $u_* = \sqrt{\tau_{\mathrm{sfc}}/\rho}$ and reads

$$u_* = \frac{\kappa s(k_{\mathrm{IB}} + 1)}{log(\Delta z_{k_{\mathrm{IB}}+1}/z_0) - \Phi(\Delta z_{k_{\mathrm{IB}}+1}/L) + \Phi(z_0/L)} \tag{16}$$

where $s(z_{k_{\mathrm{IB}}+1})$ is the speed in the grid box at $k_{\mathrm{IB}}+1$, $\Delta z_{k_{\mathrm{IB}}+1}$ is the vertical distance from the Immersed Boundary to the grid cell center of the grid box above, z_0 is the surface roughness and

$$
\begin{aligned}
\Phi(z/L) &= (1 - 16z/L)^{-1/4} & -2 < z/L < 0 \\
\Phi(z/L) &= 1 + 5z/L & 0 < z/L < 1
\end{aligned}
\tag{17}
$$

with

$$
L = -\frac{u_*^3 \theta}{\kappa g (w'\theta'_{\mathrm{V}})_{\mathrm{sfc}}}
\tag{18}
$$

where L is the Obukhov length, with θ the temperature of the surface, $\kappa = 0.4$ the von Karman constant and $(w'\theta'_{\mathrm{V}})_{\mathrm{sfc}}$ the virtual potential temperature flux of the surface.

3.1.2 Wall-bound grid boxes bound by vertical walls

The wall-bound air boxes have a heat forcing and a momentum forcing. All heat fluxes are set to zero, which is an appropriate condition for a neutrally stratified atmosphere. The momentum forcings in the vertical wall-bound air boxes are more extensive. In the DALES scheme, the subgrid flux of momentum and subgrid energy is already calculated for this grid boxes by earlier modules. Both forcings are counteracted by forcings with equal, opposite magnitude in the IBM for vertically wall-bound grid boxes, to ensure no fluxes through the walls. Next to this, a shear τ_{wall} is calculated which will be an extra τ in the momentum equation 8, to create friction.

The shear is dependent on the parallel components of the velocity to the wall. These components are defined at half a grid length from the walls. The routine DALES uses is taken from Efros (2006). Under the circumstances used in this report, the result for the wall shear τ_{wall} is

$$
\frac{|\tau_{\mathrm{wall}}|}{\rho} = \left[\frac{1-B}{2} A^{\frac{1+B}{1-B}} \left(\frac{\nu}{\Delta r}\right)^{1+B} + \frac{1+B}{A} \left(\frac{\nu}{\Delta r}\right)^{B} |s_{\mathrm{tan}}| \right]^{\frac{2}{1+B}}
\tag{19}
$$

where $A = 8.3$, $B = 1/7$, $\nu \approx 1.41 \cdot 10^{-5}$ m^{2}s^{-1}, s_{tan} is the tangential velocity and Δr is the shortest distance from the wall to the middle of the adjacent gridbox ($0.5\Delta x$ or $0.5\Delta y$). The first term on the right hand side of the equation is insignificantly small compared to the right side; when $s_{\mathrm{tan}} = 1\mathrm{ms}^{-1}$ and $\Delta r = 1$m, the right side is 1000 times larger. The stress is then proportional to $s_{\mathrm{tan}}^{\frac{2}{1+B}} = s_{\mathrm{tan}}^{7/4}$.

Efros (2006) developed this stress calculation for the buffer layer between the viscous sublayer and the inertial sublayer where Reynolds numbers are lower. This stress calculation is not validated for the Reynolds numbers used in this report. This stress calculation can be related to the stress calculation of the horizontal wall from equation 16. In figure 3 is $u_*^2 = \tau/\rho$ shown for the vertical and horizontal wall, when $(w'\theta'_{\mathrm{V}})_{\mathrm{sfc}} = 0$.
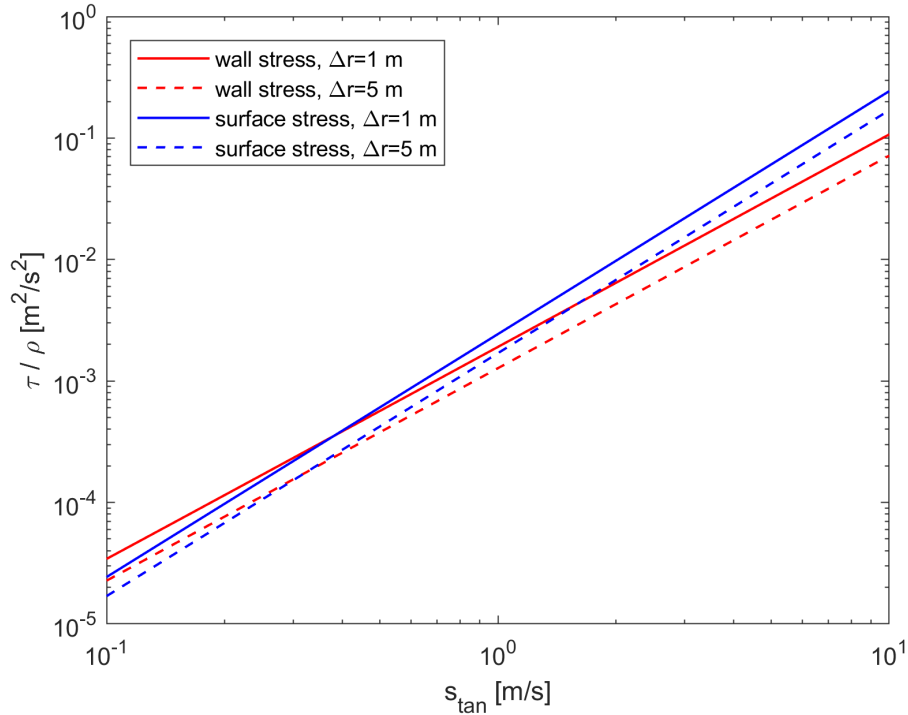
Figure 3: A comparison between the wall stress τ_{wall} and the surface stress τ_{sfc} for common atmospheric velocities. The z_0 of this example is $3 \cdot 10^{-4}$m, $(w'\theta'_{\text{V}})_{\text{sfc}} = 0$. These settings will come back later in the report.

The stresses are equal for $s_{\text{tan}} = 0.39\text{ms}^{-1}$ for a grid spacing of $\Delta x = 2$m, which means the distance from the surfaces to the center is 1m. For $s_{\text{tan}} = 10\text{ms}^{-1}$ is their difference a factor of 2.3. Their difference is even larger for larger Δr and for larger z_0.

Another adjustment in the wall-bound grid points is the use of a damping function D for the eddy viscosity. It is suggested by Piomelli and Balaras (2002) to change the eddy viscosity calculation to

$$K_{m,\text{wall}-\text{bound}} = DC_m\lambda e^{1/2}. \tag{20}$$

The free air eddy viscosity equation 13 is multiplied with a damping factor D. The damping function D is

$$D = 1 - exp[-(r^+/A^+)^3] \tag{21}$$

with $A^+ = 25$ and $r^+ = \frac{0.5\Delta r\sqrt{\tau_{\text{wall}}}}{\nu}$. This term is negligible for atmosphere flow with $\Delta r > 1$m because $r^+ > O(10^4)$.

These damping routine and the shear routine become more significant when the Reynolds number decreases.

The final difference in the wall-bound boxes is the addition of the term $\frac{\partial e_{\text{sgs}}^+}{\partial t}$ in the

subgrid energy equation 15 to the right hand side of the equation, which is

$$\frac{\partial e_{\text{sgs}}^+}{\partial t} = -K_m \frac{\partial^2 e_{\text{sgs}}}{\partial x^2}$$

$$+ \frac{K_m}{e_{\text{sgs}}} \left(-2 \left(\frac{\partial w}{\partial x} + \frac{\partial u}{\partial z} \right)^2 + \left(2\frac{\partial w}{\partial x} + \frac{\partial u}{\partial z} \right)^2 - 2 \left(\frac{\partial v}{\partial x} + \frac{\partial u}{\partial y} \right)^2 + \left(2\frac{\partial v}{\partial x} + \frac{\partial u}{\partial y} \right)^2 \right). \tag{22}$$

3.1.3 DALES-IBM difficulties

DALES-IBM has a couple of challenges in its use. The most obvious error is the restriction to a discretised immersed boundary, in contrast to TFC. The immersed boundaries can only consist of rectangular shapes, which makes it impossible in this version of IBM to use a curved wall. It is possible that the discretized hills as it is loaded into DALES acts differently than the smooth hill.

In addition, the calculation of surface fluxes is more prone to errors for hills than for flat terrain. Compared to flat surface, non-horizontal surfaces have more surface area per horizontal length that can produce fluxes such as temperature fluxes. This surface area is either overestimated if horizontal and vertical walls produce the fluxes, or it is underestimated if only the horizontal walls are taken into account in the production of these fluxes. Furthermore, these fluxes are dependent on the wind speed and the wind itself is distorted by the discretisation.

Lastly, penetration velocities occur inside of the immersed boundary, typically of the order $10^{-4}U$, U being the velocity in the wall-bound grid box. The reason is that the incompressibility equation is applied after the momentum equation. Read more in Koene (2020) and Pourquie et al. (2009).

3.2 Terrain Following Coordinates

In this study we test the IBM. Another common technique to include obstacles that can be applied is called the Terrain-Following Coordinate method (TFC). It uses the coordinates-transformation

$$z'(x,y) = h\frac{z(x,y) - z_{\text{gl}}(x,y)}{h - z_{\text{gl}}(x,y)} \tag{23}$$

where z' is the new height coordinate, h the domain height and z_{gl} the orography height. This changes the Navier-Stokes equation because of the new vertical coordinate z' and the new Navier-Stokes has to be solved. There are similar techniques that also change the z-coordinate on the basis of other properties such as the pressure. Read more about the TFC in Clark (1977) and advantages of both methods in Finardi et al. (1993) and Pourquie et al. (2009). In this report, the IBM is used, since DALES-IBM has recently been developed. An important advantage of IBM is that the height z anywhere in the domain is the geometric height. A disadvantages

lies in the the height of the ground level z_{gl}, which is an important parameter for flow around hills hills. z_{gl} is discretized for IBM, in contrast to the actual z_{gl} of any hill, and in contrast to the TFC alternative. The parameter z_{gl} will play an important role later.

4 Case set-ups

The main objective of this report is to validate the IBM-module from DALES. This is done by virtually joining the intercomparison study from (Bechmann et al. 2011). In this study various models participated in the simulation of the wind along the Bolund hill, including LES models. The results were compared to the data gathered around the hill as described by (Berg et al. 2011). An important motivation to choose this study is the availability of the observation data. The Bolund hill data were gathered under near neutral conditions. The Neutral Boundary Layer has an infinitely large Monin-Obukhov length L, because $(w'\theta'_V)_{\text{sfc}} = 0$ in equation 18. DALES has never been validated for the NBL. For this reason, the first step towards understanding the DALES-IBM results in non-flat circumstances is simulating a flat NBL in DALES. The cases to do this are described in section 4.1. The case settings for the Bolund hill simulation are described in section 4.2. Section 4.3 shortly describes the relevant output by DALES used in this report.

4.1 Case set-up flat NBL runs

The flat NBL runs were constructed for two goals and their settings will be explained separately.

Flat NBL set-up 1

The first goal is to answer the question:

- How well does DALES model the NBL for various grid settings?

The results will be compared with NBL theory and observations. The observations used are from the Bolund experiments (Berg et al. 2011). One wind mast in their research (M0) was independent of the Bolund hill and its data represents a NBL atmosphere. It collected data only if $|L| > 250$m, $5\text{ms}^{-1} < s < 12\text{ms}^{-1}$ and the angle was within 5 degrees of the desired angle $270°$ ($0°$ is true north, clockwise). Its data can be found in table 1.

Table 1: The data collected by Berg et al. (2011) that represents a flat NBL atmosphere. μ is the average and σ the standard deviation.

	z[m]	$u_*[\text{ms}^{-1}]$	$\overline{s}/u_*$	$\overline{u}/u_*$	$\overline{v}/u_*$	$\overline{w}/u_*$	$\overline{e}/u_*^2$	$\overline{u'u'}/u_*^2$	$\overline{v'v'}/u_*^2$	$\overline{w'w'}/u_*^2$
μ	5.25	0.469	22.57	22.56	0.66	-0.17	5.39	6.40	2.92	1.47
σ	-	0.070	1.71	1.70	1.51	0.12	0.67	1.02	0.64	0.13

This specific velocity profile is a function of the large scale pressure gradient but the geostrophic wind components U_g and V_g that drive this surface velocity, are unknown. It has been determined that this specific velocity is a consequence of $U_\text{g} = 16.7\text{ms}^{-1}$ and $V_\text{g} = -3.5\text{ms}^{-1}$, by extrapolating relations of other runs. The

method is critically discussed in section 5.2. The potential temperature and the surface temperature along the entire report is 288K. Pr_T is 1, following advise from de Roode et al. (2017) to minimize excessive SFS TKE production. The runs are prolonged until the results are stationary. A method to save computational time is to stretch the vertical grid size Δz. The vertical grid size for a stretched grid is

$$\Delta z(k) = \Delta z(k-1) \cdot r \tag{24}$$

with $r = 1.03$. The k from where the stretching begins is free to determine. Grids that are not stretched have $\Delta z(k) = \Delta z(1)$. The verification that stretching the grid does not influence the results is done in the second test set 7.

Table 2: The settings of the surface layer runs. All had a domain height of approximately 2560m and were vertically stretched from $k = 1$. The geostrophic wind components are $U_g = 16.7\text{ms}^{-1}$ and $V_g = -3.9\text{ms}^{-1}$.

Run	$\Delta z(1)[\text{m}]$	N_z	$\Delta x[\text{m}]$	$l_x[\text{m}]$	N_x	$z_0[10^{-4}\text{m}]$
1	10	72	10	640	64	3
2	10	72	10	3200	320	3
3	4	102	4	640	160	3
4	4	102	4	1024	256	3
5	2	124	4	640	160	3
6	2	124	4	1024	256	3
7	2	124	10	3200	320	3
8	1	147	4	640	160	3
2.2	10	72	10	3200	320	30

Flat NBL set-up 2

The simulation of the Bolund hill requests a different desired velocity profile than the velocity from the previous section. A different velocity profile in the surface layer is the result of a different geostrophic wind. The geostrophic wind is an input parameter in DALES. It is desired to find a generalization between the geostrophic wind and desired wind profiles in the surface layers. The second set-up is built to answer the question:

- Is there a general relation between the surface layer velocity and the geostrophic wind velocity?

For various (U_g, V_g) the surface layer velocities are examined to find a general relation.

Table 3: The settings for the runs used in the determination of the relationship between the geostrophic wind velocity and the wind velocity at $z = 5$m. $\Delta z(1) = 10$m. $l_x = 640$m, $\Delta x = 10$m, $N_x = 64$. $z_0 = 3 \cdot 10^{-4}$m.

Run	$U_g[\text{ms}^{-1}]$	$V_g[\text{ms}^{-1}]$	$l_z[\text{m}]$	$\Delta z(1)[\text{m}]$	Stretched
11	18.0	-13.0	1275	10	No
12	18.0	-11.0	1275	10	No
13	18.0	-9.0	1275	10	No
14	16.0	-13.0	1275	10	No
15	16.0	-11.0	1275	10	No
16	16.0	-9.0	1275	10	No
17	14.0	-13.0	1275	10	No
18	14.0	-11.0	1275	10	No
19	14.0	-9.0	1275	10	No
15.1	16.0	-11	2555	10	No
10.1	16.7	-3.9	2555	10	No
10.2	16.7	-3.9	2462	10	Yes, from $k = 1$

Run 15.1 was ran to verify whether the low l_z from run 15 results in a similar outcome as run 15.1. Runs 10.1 and 10.2 are ran to verify if a stretched grid results in equal results to a non-stretched grid. It turns out that their results are nearly equal as seen in the Appendix.

4.2 Case set-up Bolund run

The goal of the set-ups with an immersed boundary is to answer the question:

- How well does DALES-IBM model the Bolund hill for various grid settings?

The wind velocity far enough from the hill such that there is no influence from the hill will be called inflow. For the Bolund simulation is desired that the inflow is similar to the Bolund comparison case inflow from Bechmann et al. (2011). This inflow is denoted in table 4.

Table 4: Average inflow for the Bolund comparison case (Berg et al. 2011). The averages are denoted by $\overline{\cdot}$.

$z[\text{m}]$	$u_*[\text{ms}^{-1}]$	$\overline{s}/u_*$	$\overline{u}/u_*$	$\overline{v}/u_*$
5.44	0.356	24.39	21.49	11.53

The geostrophic wind input settings to obtain this inflow follow from the flat NBL results. The selected settings will be explained in section 5.2. To create an inflow equal to the desired velocity it is needed to use the stripfunction.

Stripfunction

DALES uses periodical boundary conditions. This means that all properties in the opposing sides of the domain are exactly the same, including the velocity. The effect is that the domain acts as if it were prolonged on all sides by domains that are exactly the same.

Periodical boundary conditions also mean that heterogeneity is repeated every length l_x. In this case, that would lead to a Bolund hill virtually being surrounded by other Bolund hills. The inflow would then no longer equal the desired inflow, which comes from the flat sea.

DALES has the option to a stripfunction (van Dorp 2016). This function uses the result of a run without orography (the reference run) as the input for the run with orography (the actual run). DALES nudges the boundary of the actual run to the boundary of the reference run, smoothly decreasing with a standard depth of 10 grid boxes. The inflow of the actual run is in this manner equal to the inflow of the reference run. Because the reference run is not disturbed by orography, the inflow at the actual run will be comparable to a longer domain with a flat entrance region.

Horizontal domain size

Because of the stripped boundaries it is chosen to put the Bolund hill in the middle of the domain. Kaimal and Finnigan (1994) describes multiple separation bubbles with size h that traveled more than $10h$, h being the height of the hill. Smaller bubbles travel even further. The selected horizontal domain size is therefore approximately $40h$ after and before the IB, namely roughly 1024 meters.

Surface roughness

The Bolund hill has a different surface roughness than the ocean where its inflow is coming from. In the current strip function it is not yet possible to change the surface roughness between the actual run and the reference run. The z_0 of water will be used in this simulation. The effect of z_0 on the velocity profiles is smaller if the hill is steeper (Liu et al. 2019) and the Bolund hill is steep. The importance of the z_0 of the Bolund hill itself is therefore less important than the importance of having the correct inflow, which is created with its surface having a roughness length of $3 \cdot 10^{-4}$ m.

IBM set-up

The settings for the Bolund simulations are listed in table 5.

Table 5: $U_g = 13.5\text{ms}^{-1}$ and $V_g = 3.5\text{ms}^{-1}$. $z_0 = 3 \cdot 10^{-4}\text{m}$. The vertically stretched grid starts from 30 meters. All runs had a domain height of approximately 2560m

Run	$\Delta x[\text{m}]$	$l_x[\text{m}]$	N_x	$\Delta z(1)[\text{m}]$	N_z
A	4	1024	256	1	148
B	4	1024	256	2	125
C	10	1120	112	2	125
D	10	1120	112	4	103
E	25	1200	48	4	103

Immersed Boundary

All runs need an immersed boundary file which is loaded into DALES. The hill that is modelled is the Bolund hill, whose contour map is shown in figure 4.
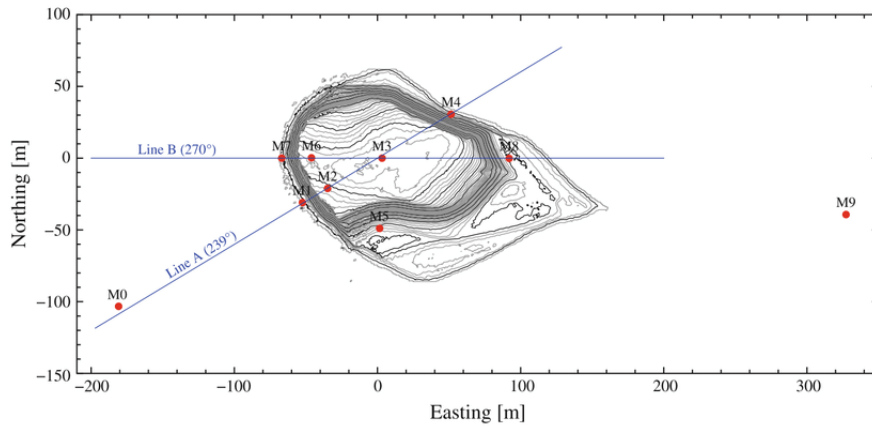
Figure 4: The Bolund contour map with $0.25\ m$ interval. The wind masts are the red dots. From (Bechmann et al. 2011).

The height of the orography as it is loaded in into DALES, $k_{\text{IB}}(i,j)$, is determined via

$$k_{\text{IB}}(i,j) = \text{round}(z_{\text{IB}}(i,j)/\Delta z) \tag{25}$$

where z_{IB} is the maximum height of the Bolund hill in the horizontal domain of (i,j).

This will lead to discretisation jumps. The $k_{\text{IB}}(i,j)$ looks like figure 5 for run B($\Delta z = 2$, $\Delta x = 4$) as example.
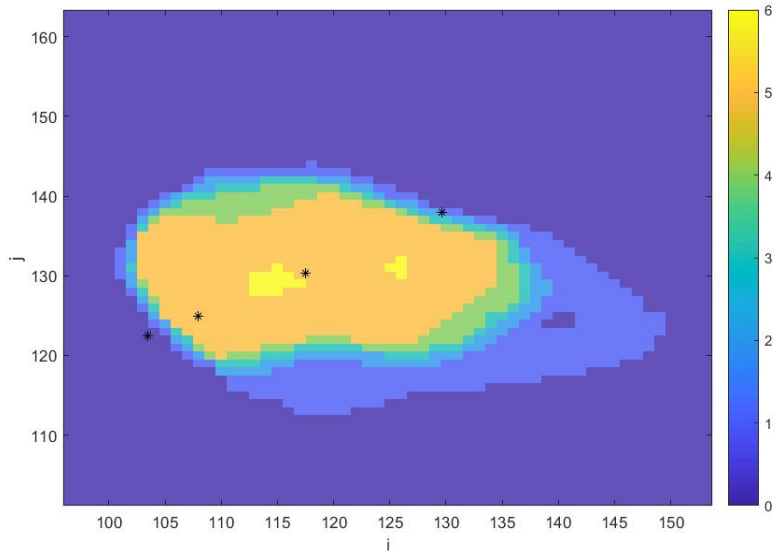
Figure 5: The Immersed Boundary $k_{\text{IB}}(i,j)$ for run B ($\Delta x = 4$, $\Delta z = 2$). The dots are masts 1 to 4.

The other immersed boundaries can be found in the Appendix.

The IBM module is not built for a stretched grid. Thus, the stretching must start from a higher k than the highest k_{sfc}. For the Bolund simulations, it is chosen to begin the stretching from $h = 30\text{m}$.

4.3 Output DALES

The output of DALES consists of slab-averaged data and instantaneous 3D fields. The slab-averaged data can be used for the flat-domain runs, but this is not possible for runs with hills, since slab averaging is no longer justified. The instantaneous velocity components and the subgrid turbulent kinetic energy will be important output. This data is collected on the locations in the grid as indicated by figure 1. The total turbulent kinetic energy (TKE) is defined as the sum of the resolved and subgrid contributions

$$e = e_{\text{sgs}} + \frac{(u_i - \overline{u_i})^2}{2} \tag{26}$$

with $\overline{u_i}$ the average of $u_i(i,j,k)$ over the time. It will play a role in the analysis of the Bolund simulation. The velocity components have to be interpolated to the center of the grids to take all variables into account at the same point.

20

5 Flat NBL wind and turbulence structure

The flat NBL runs were designed to answer how well DALES models the NBL and whether there is a generalization between the surface layer velocities and the geostrophic wind. This section is split in two parts according to those questions, with the simulation of the NBL in section 5.1 and the determination of the generalization in section 5.2.

5.1 NBL

The neutral boundary layer simulations will be compared by theory and observations. These include knowledge about the NBL height, the surface layer velocity profiles and the surface layer turbulent kinetic energy. The results are compared along these measures.

5.1.1 Domain height

The domain height in the NBL h_{NBL} is defined in this report at the height where the turbulent stress τ is at 5% of their surface value (Abkar and Porté-Agel 2013) and is

$$h_{\mathrm{NBL}} = C\frac{u_*}{f}. \tag{27}$$

C is a constant. Garratt and Hess (2002) estimates C to be $0.2 - 0.3$ and Kaimal and Finnigan (1994) 0.25 from observations. Computational models have difficulties approaching this. Andren et al. (1994) calculates C to be 0.35 with LES, Andren and Moeng (1993) reports it to be 0.5 with LES, Coleman (1999) 0.6 with DNS.

The NBL height of all eight runs varies with C being between 0.27 and 0.41 according to equation 27. This means that DALES calculates the domain height closer to the observations than other LES models from Garratt and Hess (2002).
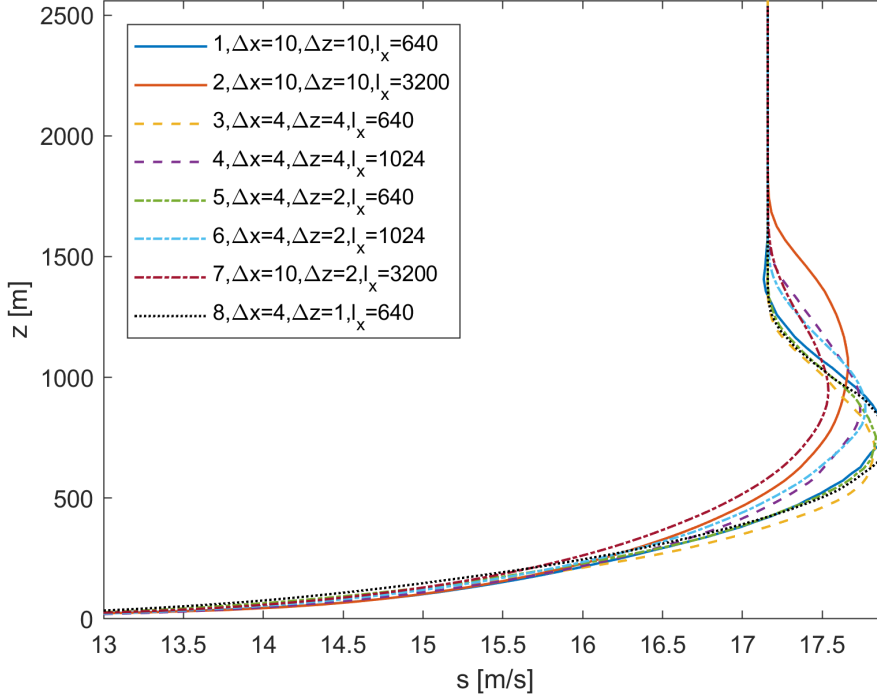
Figure 6: The vertical velocity profiles for runs 1-8 in the total ABL. The several lines are according to the legend and defines in table 2. The values in the legend have the unit of m.

The profiles in the upper part of the ABL are not convergent and group according to l_x. Runs 1, 3, 5 and 8 ($l_x = 3200$m) have the highest maximum velocity, and the respective height therefore is lowest. Runs 2 and 8 ($l_x = 640$m) have the lowest maximum velocity and the respective height therefore is highest. Runs 4 and 6 ($l_x = 1024$m) settle within. No two different l_x show the same results. Because convergence of the velocity profiles for increasing l_x has not been established yet, it is unclear what result DALES would produce for sufficiently large horizontal domain sizes. The surface layer profiles are alike, though, and more important in the rest of this report.

5.1.2 Law of the Wall

The velocity profile in the NBL in the surface layer is described by the law of the wall (LOTW)

$$s(z) = \frac{u_*}{\kappa} log\left(\frac{z}{z_0}\right). \tag{28}$$

The velocity profiles that are obtained by the runs 1-8 should approach this profile. This includes being logarithmic and having the same z_0, u_* as the desired z_0, u_*. The desired z_0 is $3 \cdot 10^{-4}$m and the desired u_* can be obtained from table 1 and is 0.469ms^{-1}. u_* is retrieved from DALES itself and the data from runs 1-8 is fitted

22

with this u_* to the LOTW to obtain a fitted z_0. The lowest 60 meters of the runs is selected for comparison. The results of those fits are shown in table 6.

Table 6: The result of the fits for run 1-8. The important grid parameters are repeated from table 2. The u_* from DALES is shown in the u_*^{DALES} column. The z_0 column shows the fitted z_0. The seventh column shows the confidence interval of z_0. The R^2 is a goodness-of-fit measure for the z_0 fit.

Run	Δx[m]	$\Delta z(1)$[m]	l_x[m]	u_*^{DALES} [ms^{-1}]	z_0 [10^{-4}m]	95 % CI [10^{-4}m]	R^2
1	10	10	640	0.45	2.0	1.3-2.7	0.93
2	10	10	3200	0.45	2.0	1.4-2.6	0.94
3	4	4	640	0.43	1.8	1.4-2.7	0.97
4	4	4	1024	0.44	1.7	1.5-2.0	0.97
5	4	2	640	0.45	3.0	2.9-3.2	0.99
6	4	2	1024	0.46	2.8	2.6-2.9	0.99
7	10	2	3200	0.49	6.1	5.5-6.8	0.96
8	4	1	640	0.46	4.8	4.6-5.0	0.99

The velocity profiles in the surface layer can be seen in figure 7 and this figure subsequently confirms the decision to select the lowest 60 meters for the fit because the velocity profiles are not affected by the upper part of the ABL yet. It can be seen that the observed wind speed at the Bolund hill does not lay on the prescribed LOTW. Their fit for z_0 was $z_0 = 6 \cdot 10^{-4}$m for this data set, but still advised $z_0 = 3 \cdot 10^{-4}$m for the simulations. This should cause a little error in the determination of u_*.

The R^2 of the z_0-fits and the z_0 confidence intervals confirm that the runs approximate the LOTW well. Runs that underestimate the u_* also underestimate z_0. It is possible to scale up the grid size to valuable results, since even the coarsest grid sizes had a reasonable R^2. The z_0 fits seem to diverge a lot from the desired z_0. Since the z_0 is part of a logarithmic function, it is actually not that far off and mostly explained by the wrong estimation of u_*.
Runs 5 and 6 (both $\Delta x = 4$m, $\Delta z = 2$m) provided the best estimation of z_0, even better than the finest grid run 8 ($\Delta x = 4$m, $\Delta z = 1$m), with a high goodness-of-fit. It can be concluded that that isotropic grids estimate z_0 better than an-isotropic grids.
Run 9 was ran to see if the results held for different z_0. It showed the same characteristics as run 2. The conclusions are thus expected to be equal for other z_0 as well.
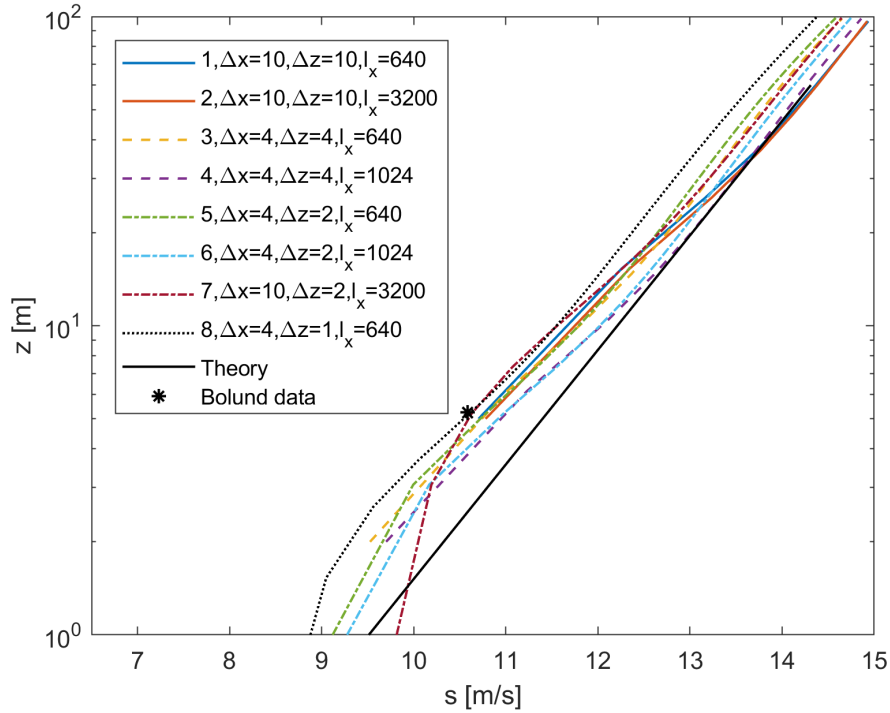
Figure 7: The simulated velocities in the lowest 60 meters compared to the Bolund LOTW on a logarithmic scale. The several lines are according to the legend and defines in table 2. The values in the legend have the unit of m. The data point is the actual measured average wind speed at mast M0. The input conditions U_g and V_g were selected such that the wind profiles match the Bolund observation.

The velocities at $z = 5$m for all runs differ with less than 3%.

Dimensionless wind shear comparison

Another measure to analyse surface layer velocities is the dimensionless wind shear Φ_M over the height. This quantity is a function of the derivative of the velocity and reads

$$\Phi_M = \frac{\kappa z}{u_*}\sqrt{\left(\frac{\partial u}{\partial z}\right)^2 + \left(\frac{\partial v}{\partial z}\right)^2}. \tag{29}$$

The Monin-Obukhov Similarity Theory predicts that $\Phi_M = 1$ over the height, but (Andren et al. 1994) showed that LES models did not approach this result.
DALES performs better than the models in Andren et al. (1994) since Φ_M is closer to one but is still significantly different than 1, as seen in figure 8.

24
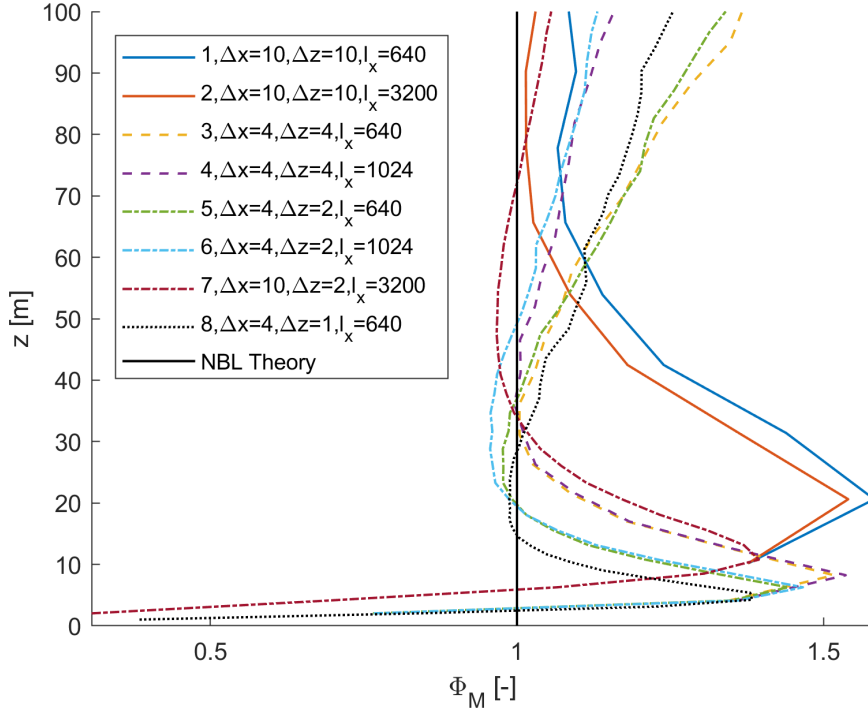
Figure 8: The dimensionless wind shear Φ_M. The several lines are according to the legend and defines in table 2. The values in the legend have the unit of m.

Runs 1 and 2, which had the coarsest meshes, do not follow the same pattern as the rest. They overestimate Φ_M for the largest part and are substantially worse than all other runs. The Φ_M of the other runs are especially between $z = 20$m and $z = 60$m close to 1. The outer part of the ABL starts to influence the velocity above $z = 60$m and Φ_M is no longer expected to follow the MOST. Under $z = 20$m there is a kink towards the lowest surface level. This kink is also observed in Ercolani et al. (2017). The reason may be the stress calculation. The stress in the lowest grid height is always purely subgrid-stress. The stress transitions from subgrid stress towards resolved stress over some height as seen in figure 9. This transition could lead to the error in $\frac{\partial s}{\partial z}$ because it coincides with the error in Φ_M.
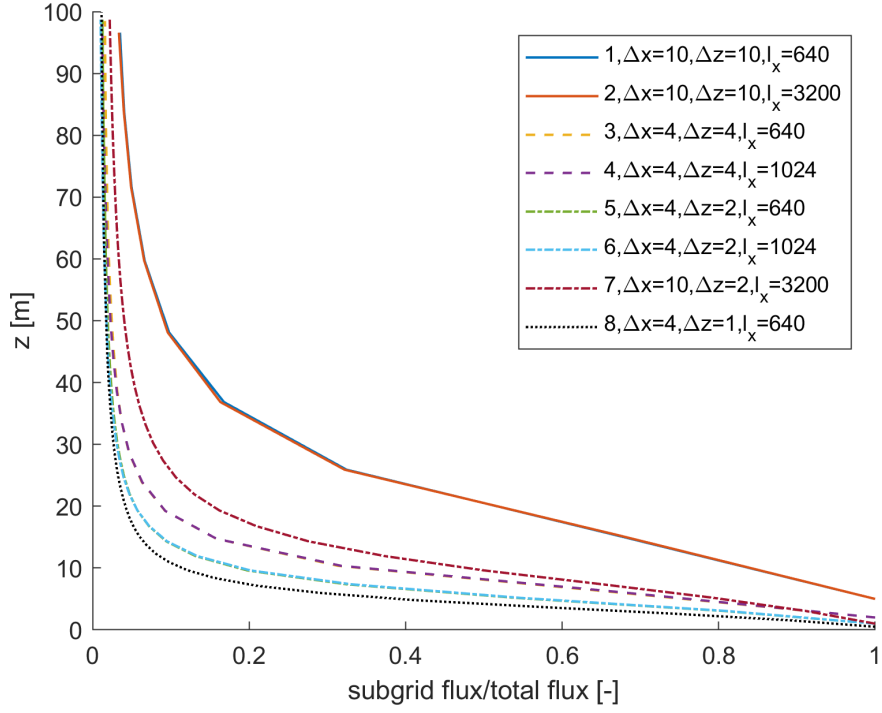
Figure 9: The share of the subgrid-flux in the total flux. The several lines are according to the legend and defines in table 2. The values in the legend have the unit of m.

Turbulent kinetic energy

The turbulent kinetic energy should be constant over the height in the NBL surface layer (Stull 1988). It should have the value of $e = (5.2 - 5.8)u_*^2$ as seen in the Bolund data. The simulated total TKE from DALES is plotted in figure 10.
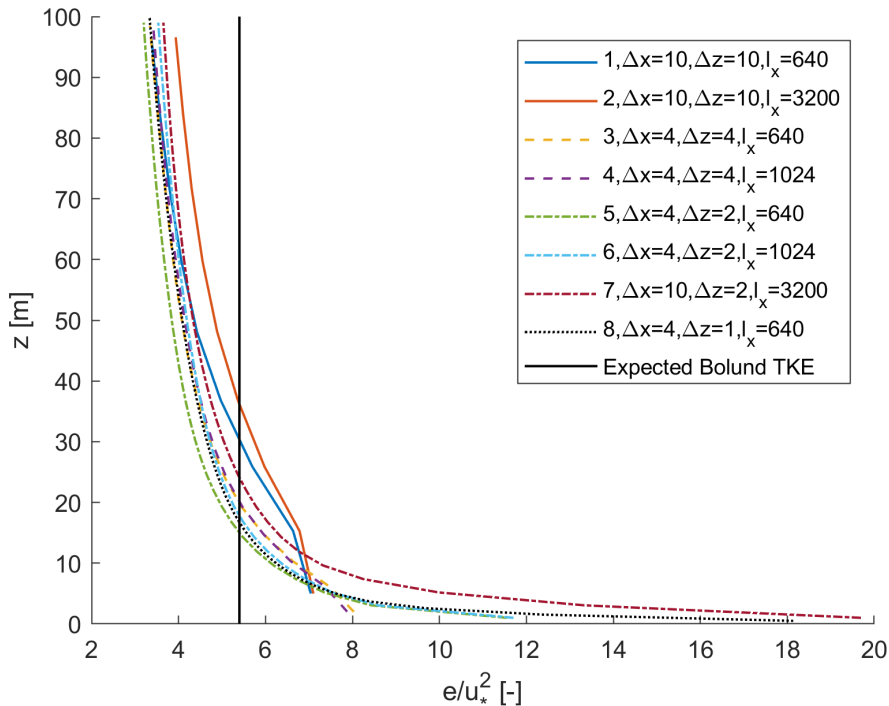
Figure 10: The results of the total turbulent kinetic energy versus the height. The several lines are according to the legend and defines in table 2. The values in the legend have the unit of m. The u_* in the x-coordinate is the friction velocity from the DALES run.

DALES is not able to capture this property of a constant e of the NBL. DALES overvalues the e in the lowest regime and explodes near the surface.

The runs 3-8 show convergence. Runs 3-8 are similar from $z = 20$m up, which is also the region where the subgrid-fluxes become insignificant as seen in figure 9. The calculated e at $z = 20$m is around the desired $5.8u_*^2$ as well. Furthermore, the runs 5, 6 and 8, which had the finest grid sizes, are similar even under 20 meters.

Interestingly, the high error in e for the finest grid sizes in the lowest grid layers is not fatal for their respective velocity profile; the runs with these grid sizes modelled the LOTW best. A possible explanation lies in the difference between subgrid and resolved TKE. The resolved TKE does not blow up near the surface and declines even a bit. The resolved TKE values are everywhere well within the reach of $(5.2 - 5.8)u_*^2$.

In Bechmann et al. (2011), models were compared by their vertical TKE profiles. The other LES models also had difficulty modelling the right e profile.

27

5.2 Geostrophic wind

The geostrophic wind is an input setting in DALES and it is desired to find a general relation between the surface layer velocity in the NBL and the geostrophic wind that drives it. The geostrophic wind settings and their subsequent velocities at $z = 5\text{m}$ are shown in figure 7. The results will at most differ 3% by using different grid sizes, as shown in the previous section.

Table 7: The average velocity at $\Delta z/2 = 5\text{m}$ for runs 11-19.

Run	$U_g[\text{ms}^{-1}]$	$V_g[\text{ms}^{-1}]$	$u[\text{ms}^{-1}]$	$v[\text{ms}^{-1}]$
11	18.0	-13.0	12.67	-5.13
12	18.0	-11.0	12.38	-3.95
13	18.0	-9.0	12.16	-2.84
14	16.0	-13.0	11.47	-5.50
15	16.0	-11.0	11.22	-4.38
16	16.0	-9.0	10.98	-3.24
17	14.0	-13.0	10.33	-5.88
18	14.0	-11.0	10.08	-4.74
19	14.0	-9.0	9.53	-3.37

(Garratt and Hess 2002) suggests a method to determine the needed geostrophic wind using u_* and reads

$$
\begin{aligned}
\frac{U_g}{u_*} &= \frac{1}{\kappa} log\left(\frac{u_*}{f z_0}\right) - A \\
\frac{V_g}{u_*} &= \frac{-B}{\kappa}
\end{aligned}
\tag{30}
$$

in case the surface velocity is aligned with the x-axis ($v = 0$). A and B are estimated from observations to be $A = 1.4$, $B = 4.5$, while LES on averages follows $A = 1.2$, $B = 2.3$ (Garratt and Hess 2002). These equation is near-linear, but not easily rotatable. Next to this, u_* and z_0 may not be known. The following relation between the geostrophic wind and the velocity at $z = 5\text{m}$ is therefore proposed.

$$
\begin{bmatrix} u(z = 5\text{m}) \\ v(z = 5\text{m}) \end{bmatrix} = \begin{bmatrix} \alpha & -\beta \\ \beta & \alpha \end{bmatrix} \begin{bmatrix} U_g \\ V_g \end{bmatrix}
\tag{31}
$$

Runs 1-9 were fitted to α and β from equation 31. The R^2 of the fit is 0.994 for $\alpha = 0.603$ and $\beta = 0.146$ and thus is the relation from equation 31 a fair generalization. Possible velocities at different heights can be related via

$$
s(z) = s(z_1) \frac{log(\frac{z}{z_0})}{log(\frac{z_1}{z_0})}.
\tag{32}
$$

with z_1 a reference height (Stull 1988). The suggested geostrophic wind relation from equation 31 can be compared to the suggestion from Garratt and Hess (2002) for the Bolund data, which can be found in short in table 8.

Table 8: The relevant data from table 1 to obtain the geostrophic wind for this surface layer velocity.

z[m]	u_*[ms^{-1}]	$\overline{u}/u_*$	$\overline{v}/u_*$
5.25	0.469	22.56	0.66

Using equation 30 results in $[U_g = 16.6\text{ms}^{-1}, V_g = -5.5\text{ms}^{-1}]$ and $[U_g = 16.9\text{ms}^{-1}, V_g = -3.0\text{ms}^{-1}]$ for observations and LES respectively. The obtained geostrophic wind by equation 31 for DALES $[U_g = 16.6\text{ms}^{-1}, V_g = -3.5\text{ms}^{-1}]$ sets within, thus DALES reproduces a relation between the surface layer and the geostrophic wind that is better than other LES models that Garratt and Hess (2002) used, but still not in full accordance to observations.

It is now possible to retrieve the geostrophic wind needed for the Bolund hill simulation. The desired velocity at $z = 5$m is $[7.65, 4.10]$ms^{-1}. The corresponding $[U_g, V_g]$ = $[13.5, 3.5]$ms^{-1}.

6 Comparison of Bolund hill simulations

The Bolund simulation is based on the research of Berg et al. (2011) and the intercomparison study of Bechmann et al. (2011). There is less theory behind flow over hills than over flat terrain, which draws more attention to the comparison with observations. The Bolund intercomparison will be explained first in section 6.1. The results are then shown in section 6.2. The differences between the DALES simulations are shown in section 6.3. The virtual participation of the best DALES simulation in the intercomparison study is included in section 6.4.

6.1 Bolund Intercomparison

The Bolund hill is a hill in Denmark that was used for extensive wind velocity data gathering by Berg et al. (2011). The Bolund hill was selected for research because it has a more challenging topography than previously studied hills. The inflow from the west comes from sea and is therefore relatively steady. The wind from the west encounters a vertical cliff of approximately 10 meters when it comes to land. The contour of the hill can be found in figure 4.

10 wind masts were installed on various critical places on the island and these masts collected data on various heights above ground level. The locations of these masts can also be found in figure 4. They were selected to capture four distinct phases of the flow over a hill: mast M1 is in front of the cliff, M2 is on the brink, M3 in the middle and M4 in the wake, when the wind comes from $239°$. The wind profile along this angle is one of the comparison cases and the line of this angle is called line A as in figure 4. The other comparison cases are the vertical profiles at the positions of the wind masts.

The relevant parameters in the research were the speed-up Δs, the angle of the wind $\theta = 270° - \tan^{-1}(u_2/u_1)$ and the normalized TKE Δe. The speed-up equation reads

$$\Delta s = \frac{s(x, z_{\mathrm{agl}}) - s_0(z_{\mathrm{agl}})}{s_0(z_{\mathrm{agl}})} \tag{33}$$

with z_{agl} the height above ground level and s_0 the reference wind speed which is the wind sufficiently far from the hill such that there is no influence. The normalized TKE equation reads

$$\Delta e = \frac{e(x, z_{\mathrm{agl}}) - e_0(z_{\mathrm{agl}})}{s_0(z_{\mathrm{agl}})^2} \tag{34}$$

where $e_0(z_{\mathrm{agl}})$ is the reference turbulent kinetic energy from sufficiently far from the hill such that the hill does not influence it. The turbulent kinetic energy is divided by the reference velocity to be a dimensionless parameter.

The relevant height parameter is z_{agl}. $z_{\mathrm{agl}} = z - z_{\mathrm{gl}}$, where z_{gl} is the height of the ground level, in this case the Bolund hill height.

The DALES simulations however cannot have the same z_{gl} profile as the Bolund hill, since the DALES Immersed Boundary height is discretized. The DALES Immersed Boundary height is called h_k.

The runs will have different h_k since their dimensions are different. The height h_k that the discretised immersed boundaries correspond to along line A from the contour map 4 can be seen in figure 11.
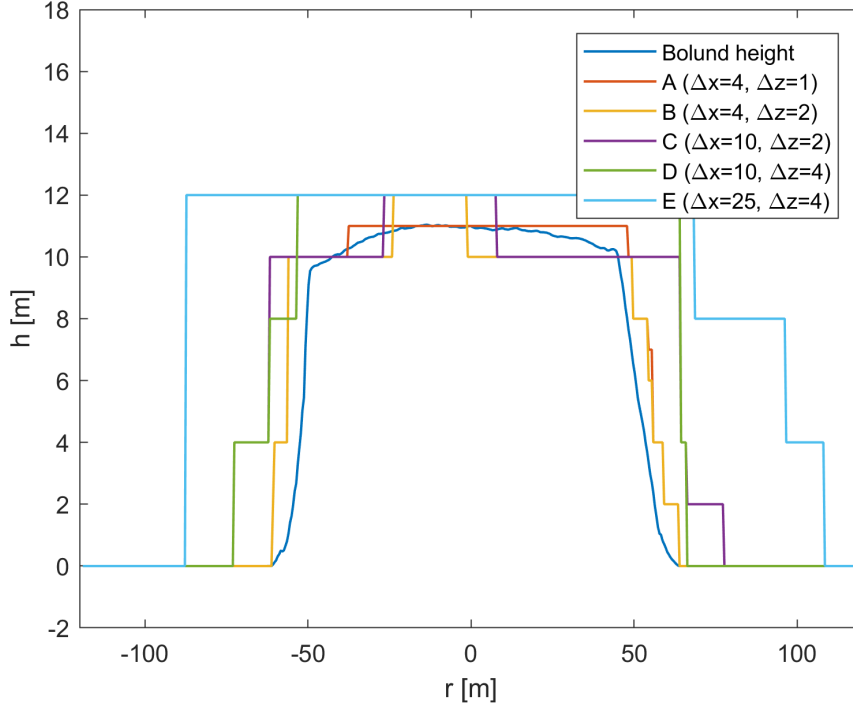
Figure 11: The immersed boundary height h_k for runs A-E along line A from figure 4 compared the actual height for the Bolund hill. The distance parameter along the x-axis will be called r in accordance with the Bolund contour figure 4. The values in the legend have the unit of m.

The r-coordinate of the wind masts M1-M4 is [-61, -41, 3, 60] m respectively.

The different h_k will cause differences for the simulated wind between the runs. It can already be seen that the immersed boundary of run E rises earlier than those of the rest, due to the grid size $\Delta x = 25$m. For the smaller grid sizes, the most significant different is the discretization of the top of the Bolund hill. The h_k from runs B and C have a small, high bump on the top side compared to a broader, lower bump from run A.

For the horizontal profile figures in this report, it is decided to use $z_{agl} = h_k$, while for the vertical profile figures, $z_{agl} = z_{agl,Bolund}$ is used.

6.2 DALES results

First, the results are presented in accordance with the shown profiles in the inter-comparison. These include the horizontal profiles of the three variables Δs, Δe and the angle of the velocity. These are shown along line A for $z_{agl} = 2$m and $z_{agl} = 5$m and vertically at the locations of masts M1-M4. In all figures, the corresponding data from the wind masts is allocated by a black circle.

(a) $z_{agl} = 2$m.

(b) $z_{agl} = 5$m.
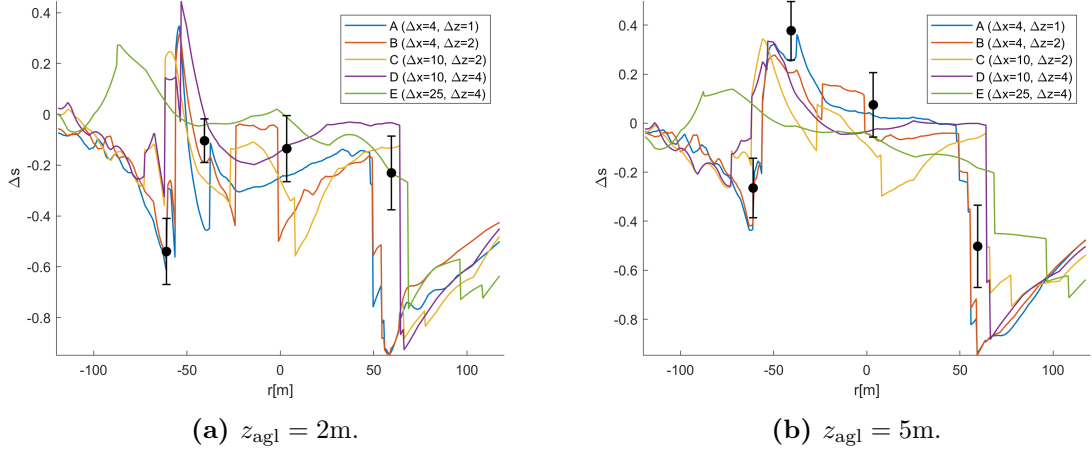
Figure 12: Speed-up Δs of the wind, as defined in equation 33, along line A for runs A-E, as defined according to table 5 in section 4. The circles correspond to the Bolund data including its uncertainty. The values in the legend have the unit of m.

(a) $z_{agl} = 2$m.

(b) $z_{agl} = 5$m.
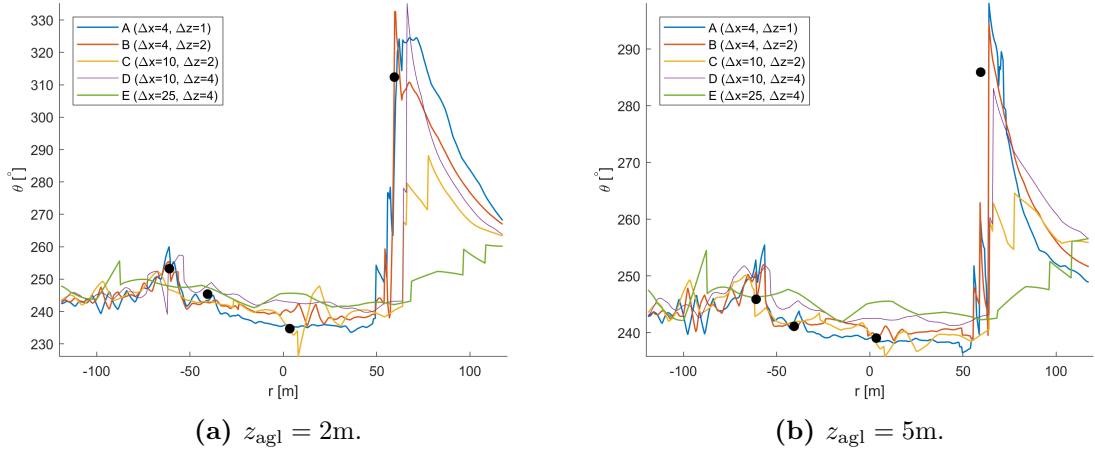
Figure 13: Angle of the wind along line A for runs A-E, as defined according to table 5 in section 4. The circles correspond to the Bolund data. The values in the legend have the unit of m.

(a) $z_{agl} = 2$m.

(b) $z_{agl} = 5$m.
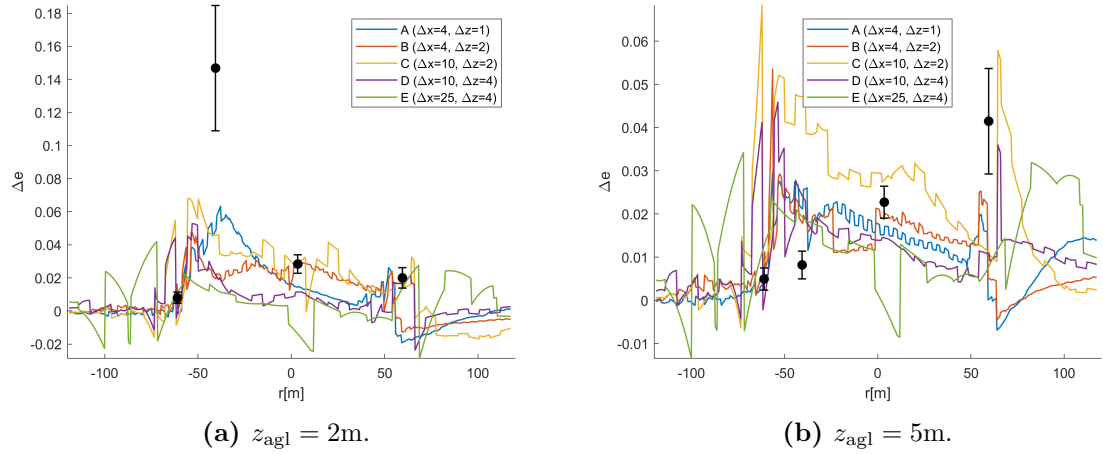
Figure 14: Normalized TKE Δe of the wind, as defined in equation 34, along line A for runs A-E, as defined according to table 5 in section 4. The locations of the masts can be seen in figure 4. The circles correspond to the Bolund data including its uncertainty. The values in the legend have the unit of m.
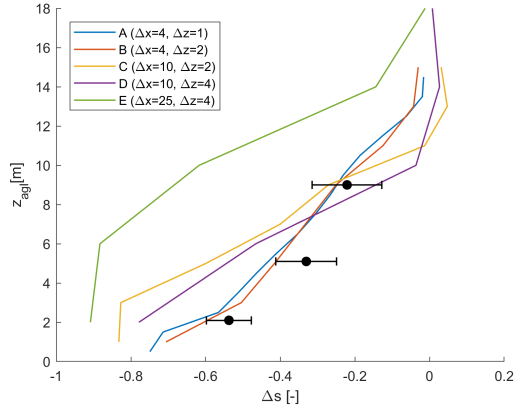
(a) Run A-E Mast 1 speedup
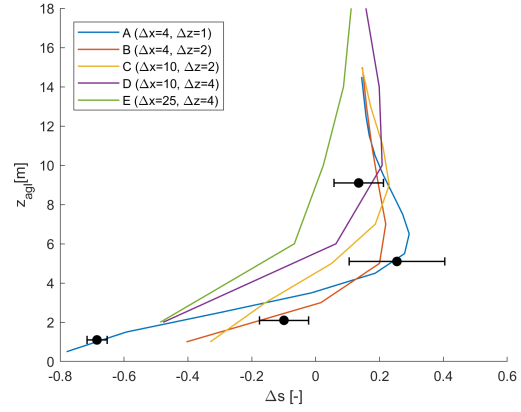
(b) Run A-E Mast 2 speedup
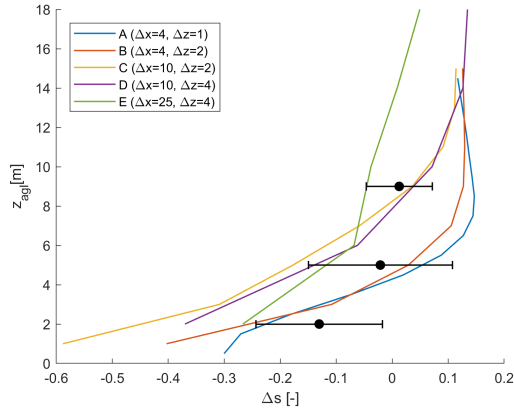
(c) Run A-E Mast 3 speedup
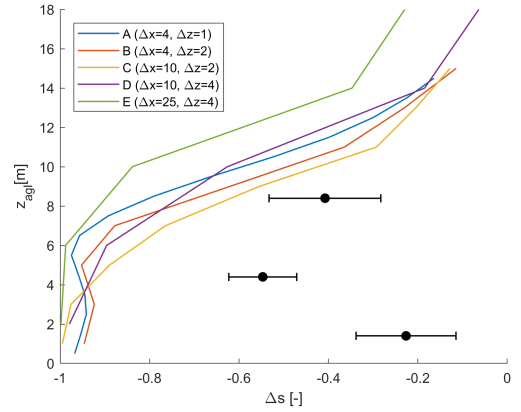
(d) Run A-E Mast 4 speedup

Figure 15: Speed-up Δs of the wind, as defined in equation 33, at the locations of Masts 1-4 for runs A-E, as defined according to table 5 in section 4. The locations of the masts can be seen in figure 4. The circles correspond to the Bolund data including its uncertainty. The values in the legend have the unit of m.

(a) Run A-E Mast 1 Δe

(b) Run A-E Mast 2 Δe

(c) Run A-E Mast 3 Δe

(d) Run A-E Mast 4 Δe
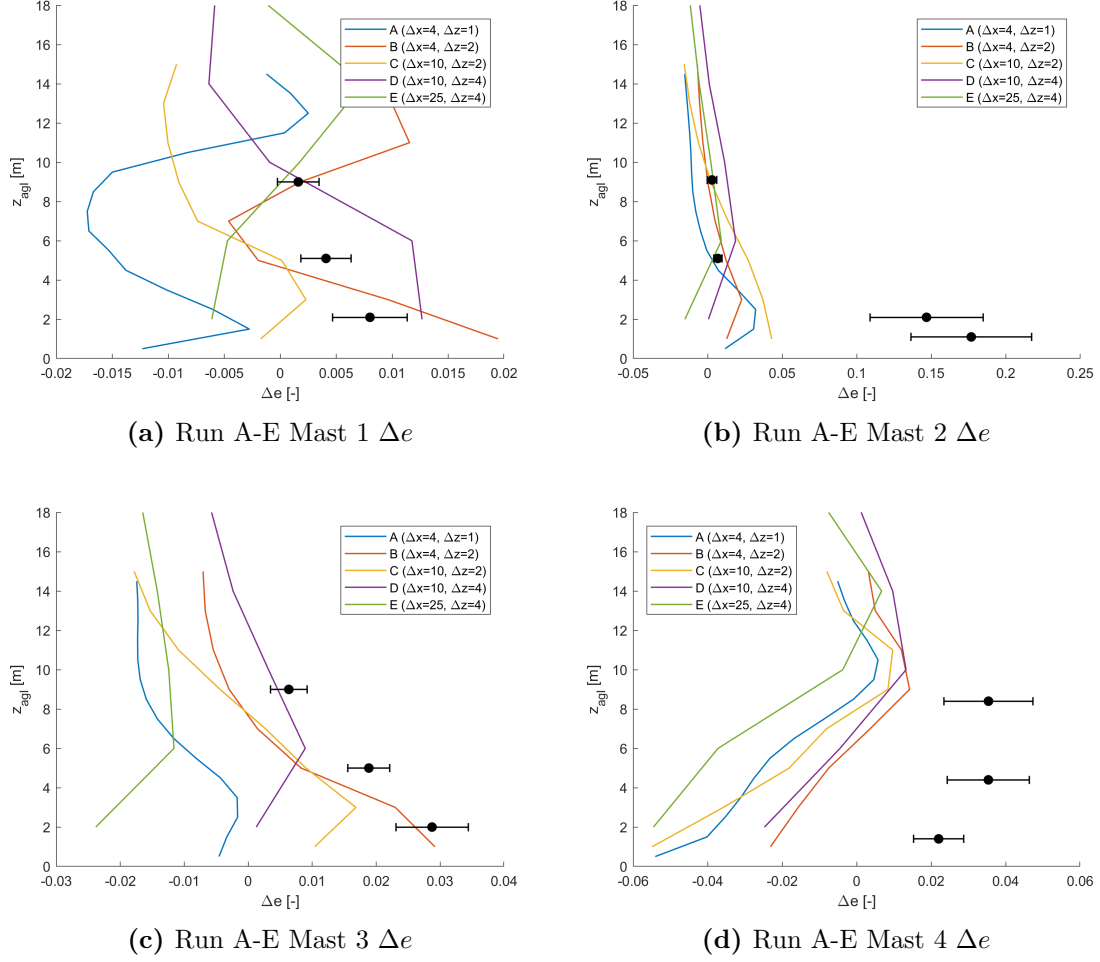
Figure 16: Normalized TKE Δe of the wind, as defined in equation 34, at the locations of Masts 1-4 for runs A-E, as defined according to table 5 in section 4. The locations of the masts can be seen in figure 4. The circles correspond to the Bolund data including its uncertainty. The values in the legend have the unit of m.

6.3 Convergence runs A-E

The differences between run A ($\Delta x = 4$m, $\Delta z = 1$m) and B ($\Delta x = 4$m, $\Delta z = 2$m) are for the largest part insignificant. There are two significant differences. The first is the speed-up on top of the hill, which can be seen in figure 12 between $r = -50$m and $r = 20$m. This region is the only region where their immersed boundary height h_k differ. In both cases does the h_k increase one last step on the hilltop plateau. For both does the speed-up rapidly decrease in front of this step, and increase once h_k is higher. The decrease is caused by the blockade upwind and the increase because the speed-up is measured at a higher z_{agl}. Interestingly are the profiles of run A and B downwind from $r = 20$m resembling and did the earlier differences not cause permanent differences.

The other significant difference can be found in the normalized TKE profiles. Δe

35

is lower everywhere for run A, especially in the lowest grid levels. The reference TKE e_0 of run A is much higher than of run B. This could also be seen in figure 10, because run A has the same grid sizes as run 8. Run B, which had the same grid sizes as run 6, stayed closer to the expected e_0. Its Δe results are therefore better in the lowest regions.

Run C ($\Delta x = 10\text{m}, \Delta z = 2\text{m}$) still has comparable results to run A and B. The speed-up profiles relate closely to those of run A and run B. However, the Δe profiles differ in two manners. The drop on the leeward side is gone. Larger grid sizes have inherently more subgrid contribution and there is more downward wind w. This pushes more wind over the edge downward and thus is the wind direction closer to $239°$ than runs A and B. The reference TKE e_0 is too high, just like its fellow an-isotropic grid run A.

The results of run D ($\Delta x = 10\text{m}, \Delta z = 4\text{m}$) is still within reasonable ranges of runs A and B. Its Δe profiles are typically somewhat lower than those of run C, because grid sizes are larger and thus derivatives smaller. Its speed-up profiles are still quite similar to A-C. The most significant speed-up error is the inability to capture the drop in speed-up in front of the ridge.

Run E ($\Delta x = 25\text{m}, \Delta z = 4\text{m}$) is the first run characterised by wrong Δe profiles and unreliable lower levels in the vertical profiles. The fluxes are dominated by subgrid contributions and these are not accurate. The speed up profiles still vaguely resemble the profiles of run A, but the hill has broadened almost 50 meters due to the discretization. The areas in front of the hill and at the back of the hill are therefore no longer comparable.

6.4 Comparison Bolund paper

The results from run B are best and will be taken into account for the virtual participation in the Bechmann et al. (2011) paper. This section is thus solely about the results of run B. Run B is performing decent in the Bechmann et al. (2011) paper. Its virtual participation will be divided into its absolute error calculation and a comparison by its horizontal and vertical profiles.

Absolute error at wind masts M1-M4

DALES-IBM models the speed-up reasonably good and it has a little more difficulty modelling Δe. The mean error for the simulated speed-up R_S can be calculated using the wind mast data.

$$R_\text{S} = |\Delta s_\text{S} - \Delta s_\text{m}| \tag{35}$$

with the subscript S for the simulated, DALES, result and the subscript m for the measured speed-up. R_S is 0.154 for M1-4 and 0.061 for only M1-M3 for run B. The

average in the intercomparison is only given for this case together with a similar case. The models on average score 0.173. The mean results are therefore slightly better than average, but the results are mast-dependent. The simulated speed-up at M1-3 are superior to the other models.

The absolute normalized TKE error reads

$$R_{\text{TKE}} = |\frac{\sqrt{e_{\text{S}}} - \sqrt{e_{0,\text{S}}} - (\sqrt{e_{\text{m}}} - \sqrt{e_{0,\text{m}}})}{\sqrt{e_{0,\text{m}}}}| \tag{36}$$

with the subscript 0 for the reference value on the inflow is 0.55 and slightly worse than average, which is 0.50.

Speed-up profiles

The speed-up profiles of run B show mostly the same tendencies as the other participants do and as the Bolund data shows. The speed-up in front of the hill is calculated appropriately and the speed-up on the hill edge as well. The maximum speed-up is in agreement with theory from (Kaimal and Finnigan 1994) as well, that states that the maximum speed-up should be approximately

$$\Delta s_{\text{max}} = 1.25 h/L_h \tag{37}$$

where L_h is the distance from the crest to the half-height point which is approximately 70 meters. The maximum speed-up is then 0.2. The speed-up along the ridge at $z_{\text{agl}} = 2\text{m}$, figure 12, is decreasing faster than most other other models do. It is however in agreement with the data from the wind masts along line A. DALES-IBM has the most difficulty representing the profiles around mast M4 from $r = 50\text{m}$. The hill is steep here and the wind in the lower regions will flow along the north side of the hill. DALES however creates a tail along the A-line directly after the Bolund hill with hardly any wind and any turbulence. This can also be seen in the speed and velocity figures 17.

(a) Velocity $\overline{s}$

(b) TKE $\overline{e}$
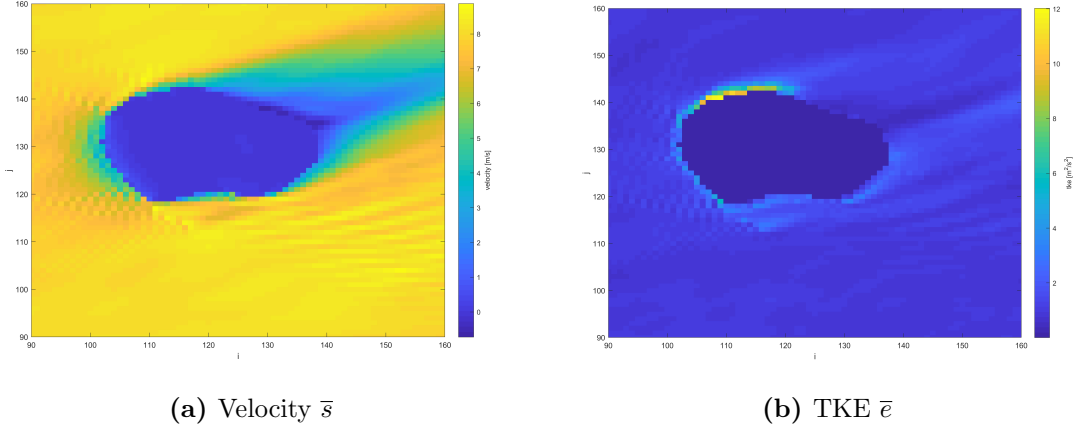
Figure 17: The averaged velocity and TKE profiles close to the Bolund hill for run B for $k = 3$.

The low pressure region after an obstacle will normally cause turbulence Kaimal and Finnigan (1994) and DALES-IBM does not capture this. This could be a consequence of the low τ_{wall}. The velocities along the walls are a little too high because the wall creates too little shear. The air consequently passed the wake, and due to little produced shear does the wind also contain less SFS TKE than if more shear was produced.

The w-profiles of mast M4 are shown in figure 18. The vertical velocity is positive for the $z_{\mathrm{agl}} = 2$m. This is a sign that separation is occurring, because non-separated fluid flow typically drops after an obstacle. The DALES simulation has a positive w for the lowest z_{agl}, but far too little to create w for a substantial recirculation bubble. The reason could be the underestimation of the downward velocity w at larger heights. This could push wind towards the recirculation bubble, creating the inertia the bubble needs.

One of the causes for a downward velocity w behind a hill is the term $+\dfrac{\partial K_m \left(\frac{\partial \widetilde{u_i}}{\partial x_j} + \frac{\partial \widetilde{u_j}}{\partial x_i} \right)}{\partial x_j}$ in the momentum equation 8, since $\frac{\partial^2 \widetilde{u_i}}{\partial x_j^2}$ is negative. It can be seen in figure 16d that Δe is too low at the hilltop height. The low TKE causes a low K_m, which causes too little downward velocity. This could again be a result of the low wall shearing.
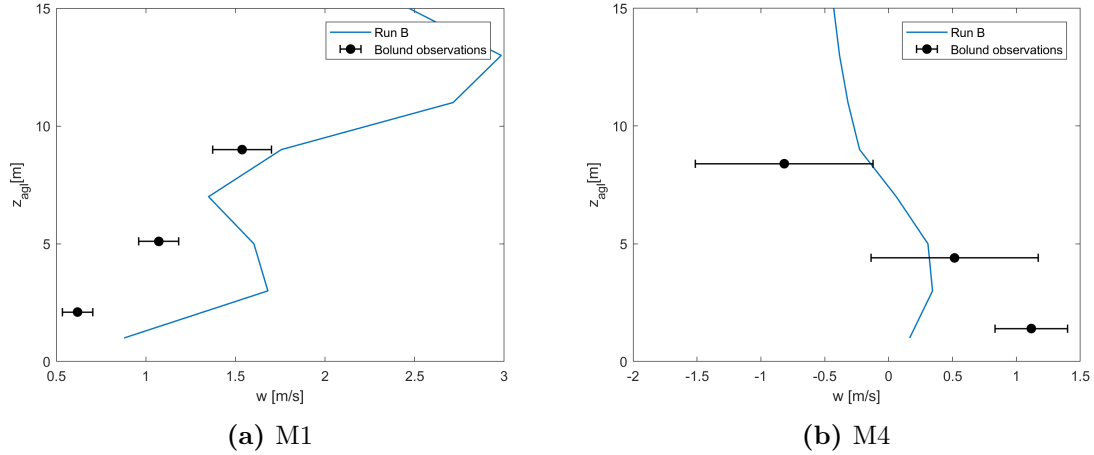
Figure 18: The averaged vertical velocity w at the position of masts M1 and M4 and the Bolund observation.

The vertical velocity in front of the hill is too high, although the slight change in wind direction at the front of the hill is correctly captured. The wrong w could be caused by wrong shear calculations. When the shear is too little, this causes too little deceleration, resulting in too high vertical velocities.

Horizontal normalized TKE profiles

The horizontal Δe profiles of DALES do not approach the Bolund data as seen in figure 14. The errors that have not been discussed are the underestimation of the TKE for $z_{\mathrm{agl}} = 2$m at $r = -42$m on the edge of the hill, which should be more than twice as high and the decrease of normalized TKE along the ridge in the DALES simulation while the observed TKE increases. The underestimation on the edge could be a consequence of too little shearing as the wind rises along the escarpment. The updraft of wind is indeed too high in DALES compared to the results as shown in figure 18 and the TKE is a little too low.

A reason that the values are typically too low on the edge is the used z_0 in the simulation. The hill in DALES acts as if it has the surface roughness of water. DALES then wrongfully calculates the τ_{sfc}. Next to this, the updrafted TKE diffuses along the wind. Since the updrafted TKE is underestimated, it is not possible to diffuse this TKE in DALES.

The Δe along the ridge is difficult to compare, because the bump in h_k causes too much change compared to the actual Bolund Δe that creates unreliability in the results.

Vertical normalized TKE profiles

The vertical Δe profile at M3 is in accordance to the Bolund data. DALES underestimates the Δe at M4 as it is in the wake, although it estimates Δe much better above $z_{agl} = 10$m. The normalized TKE at M1 and M2 are off. The simulated TKE at M1 has a fluctuating profile while the Bolund data does not have that. The escarpment rises in stages in the simulation. This could cause those fluctuations because of non-smooth flow along the escarpment. The TKE at M2 is off because DALES did not capture the updrafted TKE along the escarpment well. This was also discussed in the horizontal TKE profile section.

7 Discussing the Bolund simulation

The discussion is started by a note of the other LES models in the intercomparison. Afterwards, the topics of interest within the scope of the simulation are grouped: some remarks concerning the simulation itself are discussed first, the shear model is discussed second and the effects of the discretization third. The possibilities of improvement of the IBM out of the scope of this research are bundled by a moist and temperature section and the remainder.

Other LES models simulating Bolund

There were 6 LES models that took part in the original intercomparison. They performed worse than the 2-equation RANS models. Three of these 6 LES models used laminar inflow and an unspecified number of LES models were zonal LES-models. These zonal LES-models are actually closer to RANS simulations. It is unclear whether the LES models used TFC or IBM, but the absence of discretization jumps suggests that the few true LES models used TFC. Diebold et al. (2013) later modelled the Bolund hill with LES-IBM substantially better than average and better than DALES-IBM. They used a different shear model than DALES, which emphasises that a fault may lie in the DALES shearing calculation.

General Bolund simulation remarks

A possibility to improve the simulation is a change of boundary conditions. The stripfunction influences the result, especially in the tail of the wake. The results here are pushed towards a flat velocity profile, while it may still be influenced by the hill. A forced inflow instead of developing one via the cyclic boundaries is suggested for better research possibilities to the wake. This is in development. Another solution is to increase l_x.
Next to this, the surface roughness is heterogeneous around the Bolund hill. DALES has the option for heterogeneous surface roughness but this has not been adapted for the stripfunction, where the reference run (that is flat and produces the inflow) should have a different surface roughness than the actual run (that has the immersed boundary). The connection of IBM with the heterogeneous surface roughness is important since hills typically consist of multiple surface types with different surface roughness.

Shear in the IBM

The shear along vertical walls is for IBM for the Bolund simulation more than twice as small as the horizontal shear under the conditions of the Bolund simulation. A smaller shear leads to less deceleration and thus the overestimation of velocities, which indeed happened on several spots along the Bolund hill. The horizontal wall

shear τ_{sfc} from equation 16 is based upon theory that is built for the Reynolds numbers of simulations like these. The vertical wall shear τ_{wall} from equation 19 is not. The friction coefficient along the vertical walls, which is proportional to τ/s_{tan}^2, is proportional to $s_{\text{tan}}^{-0.25}$ for the vertical walls. At Reynolds numbers $> 10^6$, these changes for the friction coefficient are no longer expected (Khan et al. 2018). Furthermore, τ_{wall} is a function of $\Delta r^{-0.25}$ and as the IBM will be used for larger domains, this term will become even smaller. A better shear model needs to be implemented for the vertical walls. A model based on the the friction calculations for the horizontal walls is advised as there is theory to back this.

Discretization errors

The results are negatively affected by the non-smoothness of the immersed boundary height h_k. This is clearly visible in figure 12 in the difference between the run A and B speed-up at the hilltop and in the plots of the larger grid sizes for Δe. The speed-up profiles however were similar for runs A-D in terms of the speed-up in front of the escarpment and just above it and the vertical profiles were similar throughout. Simulating velocity profiles around hills is thus still acceptable for $L_x/\Delta x = 13$, L_x being the length of the hill and $h/\Delta z = 3$, which were the settings for run D. The Δe profiles never showed good convergence, but eventually did the isotropic run outperform a finer an-isotropic run. It is thus recommended to keep the grid isotropic if the TKE matters.

The non-smoothness of the IB-file might cause errors for hills with gradients different than $90°$. In this report most gradients were either $0°$ or $90°$, because the escarpment was near $90°$ at the front of the hill. Possible errors for different gradients are not substantially applicable in the Bolund simulations and could not be investigated. An improvement to reduce discretization errors might be found in Bao et al. (2018). A thinner grid of the orography can be loaded into DALES. The velocity in the grids next to the walls are interpolated on a logarithmic scale with the use of the distance between the grid and the closest orography-point. In this manner can the wind 'feel' an orography different than rectangular.
This method could also solve the difficulty of surface parametrisations of temperature fluxes.

Absence of moist and temperature fluxes

This research has been done with the assumption that no moist was present in the atmosphere and that the atmosphere was neutrally stratified. DALES is therefore unvalidated for the moist and temperature fluxes in hilly terrain. A possible reference case could be the Panosetti et al. (2016) paper.
The calculation of the moist and temperature fluxes for IBM in DALES are not

as developed as those of the shearing fluxes at this moment. The temperature parametrisations on the horizontal walls are for instance all based on one temperature setting. Certain parts of the hills might have different surface temperatures due to radiation or non-neutral stability conditions.

Other possible improvements

The main goal of this research was to evaluate the wind profiles around a hill to validate DALES-IBM. The effect of hills on the downwind profiles are yet to be evaluated. This is important research considering orography if the results of a combination of hills is to be evaluated.

DALES has the option to scale the K_m to a different length parameter λ_{Mason}. Now, λ is the grid length $(\Delta x \Delta y \Delta z)^{1/3}$, but is can be switched to a length dependent on κz with the Mason length scale (read more in de Roode et al. (2017)). This could potentially solve the excessive mining of e_{sgs} at the surface because it decreases the subgrid flux (Mason 1989). The surface eddy viscosity is then improved. However, this method is not integrated into IBM yet. The κz can be replaced with κr, r being the distance to the wall.

The poisson solver, which solves the mass conservation equation, is applied after the momentum equation. This leads to the small penetration velocities inside immersed boundaries. It might be possible to let the poisson solver know what grids to skip.

8 Conclusion

The conclusions of this paper can be divided into conclusions over the NBL simulation and over the Immersed Boundary Method.

The NBL simulations of DALES converged into the theoretical result for the surface layer.

The surface layer velocity profiles in the NBL are all near-logarithmic, but in the transition from the parameter-based lowest grid height to the resolved velocities in the higher regions does the dimensionless wind shear Φ_M make a kink to approximately 1.5 for all geometries. This part of the surface layer is subgrid dominated. The simulation also overestimates the subgrid turbulent kinetic energy in this part. Using an anisotropic grid enhances the excessive production of SFS-TKE and diverges the velocity from the LOTW even more.

The velocity profiles in the upper part of the ABL are strongly dependent on the domain width l_x/h and convergence has not been found. Runs with broader domain widths had a higher h_{NBL}. The surface layer velocity and TKE are not dependent on l_x.

Runs with grid sizes from $\Delta x = \Delta z = 4$m and smaller are simulating the correct turbulence structure in the surface layer. Coarser grid sizes will diverge the velocity profiles from the desired logarithmic velocity profiles. The NBL results were used to develop a relation between the surface layer velocity and the geostrophic wind components U_g and V_g. This relation can be approximated as linear. The found relation is in close agreement with (Garratt and Hess 2002) and is consistent in DALES for grid sizes up to $\Delta x = \Delta z = 10$m.

The Immersed Boundary Method module in DALES is a good method to model the velocity profiles in front of hills and along hills like the Bolund hill in NBL conditions. The results around the Bolund hill are good and better than the average model in (Bechmann et al. 2011) in front of the hill and on the ridge.

DALES-IBM is not suitable now to solve the dynamics in the wakes behind hills. The problem of the wake dynamics has to be solved before IBM can be used in situations where multiple hills or buildings succeed one another. It could potentially be the cause of the wrong τ_{wall} calculations.

The TKE profiles are more off than the speed-up profiles and slightly more off than the average model from the intercomparison.

The speed-up results are less volatile to changing grid sizes than the TKE. For the speed-up is the simulation with $\Delta x = 10$m, $\Delta z = 4$m still good. This suggests that the ratios of horizontal hill length to horizontal mesh size of $L_x/\Delta x = 13$ and hill height to vertical mesh size $h/\Delta z = 3$ are acceptable, while the suggestion is to use $L_x/\Delta x = 36$, and $h/\Delta z = 6$ to minimize the TKE errors, because only $\Delta x = 4$m, $\Delta z = 2$m performs acceptable.

Acknowledgements

9   References

Abkar, M. and F. Porté-Agel, 2013: The effect of free-atmosphere stratification on boundary-layer flow and power output from very large wind farms. *Energies*, **6**, 2338–2361.

Andren, A., A. Brown, J. Graf, P. Mason, C. Moeng, F. Nieuwstadt, and U. Schumann, 1994: Large-eddy simulation of a neutrally stratified boundary layer: A comparison of four computer codes. *Quarterly Journal of the Royal Meteorological Society*, **120**, 1457–1484.

Andren, A. and C. Moeng, 1993: Single-point closures in a neutrally stratified boundary layer. *American Meteorlogical Society*, **50**, 3366–3379.

Bao, J., F. Chow, and K. Lundquist, 2018: Large-eddy simulation over complex terrain using an improved immersed boundary method in the weather research and forecasting model. *American Meteorlogical Society*, **146**, 2781–2797.

Beare, B., et al., 2006: An intercomparison of large-eddy simulations of the stable boundary layer. *Boundary-Layer Meteorology*, **118**, 247–272.

Bechmann, A., N. N. Sorensen, J. Berg, J. Mann, and P. Réthoré, 2011: The bolund experiment, part ii: Blind comparison of microscale flow models. *Boundary-Layer Meteorol*, **141**, 245–271.

Berg, J., J. Mann, A. Bechmann, M. S. Courtney, and H. E. Jorgensen, 2011: The bolund experiment, part i: Flow over a steep, three-dimensional hill. *Boundary-Layer Meteorology*, **141**, 219–243.

Castro, F., J. Palma, and A. Lopes, 2003: Simulation of the Askervein flow. Part 1: Reynolds averaged Navier-Stokes equation. *Boundary-Layer Meteorology*, **107**, 501–530.

Clark, T., 1977: A small-scale dynamic model using a terrain-following coordinate transformation. *Journal of Computational Physics*, **24**, 186–215.

Coleman, G., 1999: Similarity statistics from a direct numerical simulation of the neutrally stratified planetary boundary layer. *Journal of the Atmospheric Sciences*, **56**, 891–900.

Dai, Y., S. Basu, B. Maronga, and S. de Roode, 2021: Addressing the grid-size sensitivity issue in large-eddy simulations of stable boundary layer. *Boundary-Layer Meteorology*, **178**, 63–89.

de Roode, S., H. Jonker, B. Van de Wiel, V. Vertregt, and V. Perrin, 2017: A diagnosis of excessive mixing in smagorinsky subfilter-scale turbulent kinetic energy models. *American Meteorological Society*, **74**, 1495–1511.

De Wekker, S. F. and M. Kossmann, 2015: Convective boundary layer heights over mountainous terrain—A review of concepts. *Frontiers in Earth Sciences*, **3**, 1–22.

Diebold, M., C. Higgins, J. Fang, A. Bechmann, and M. B. Parlange, 2013: Flow over Hills: A Large-Eddy Simulation of the Bolund Case. *Boundary-Layer Meteorology*, **148**, 177–194.

Efros, V., 2006: Large Eddy Simulation of Channel Flow using Wall Functions.

Ercolani, G., C. Gorlé, C. Corbari, and M. Mancini, 2017: Rams sensitivity to grid spacing and grid aspect ratio in large-eddy simulations of the dry neutral atmospheric boundary layer. *Computers and Fluids*, **146**, 59–73.

Finardi, S., G. Brusasca, M. G. Morselli, F. Trombetti, and F. Tampieri, 1993: Boundary-layer flow over analytical two-dimensional hills: A systematic comparison of different models with wind tunnel data. *Boundary-Layer Meteorology*, **63 (3)**, 259–291.

Garratt, J. and G. Hess, 2002: The Idealised, Neutrally Stratified Planetary Boundary Layer. *Encyclopaedia of Atmospheric Sciences*, **1**, 262–271.

Heus, T., et al., 2010: Formulation of the Dutch Atmospheric Large-Eddy Simulation (DALES) and overview of its applications. *Geoscientific Model Development*, **3 (2)**, 415–444.

Kaimal, J. and J. Finnigan, 1994: *Atmospheric Boundary Layer Flows*. Oxford University Press, New York.

Kent, C. W., C. S. Grimmond, D. Gatey, and J. F. Barlow, 2018: Assessing methods to extrapolate the vertical wind-speed profile from surface observations in a city centre during strong winds. *Journal of Wind Engineering and Industrial Aerodynamics*, **173**, 100–111.

Khan, M. H., P. Sooraj, A. Sharma, and A. Agrawal, 2018: Flow around a cube for Reynolds numbers between 500 and 55,000. *Experimental Thermal and Fluid Science*, **93**, 257–271.

Koene, M., 2020: Implementation of the immersed boundary method in the dutch atmospheric large-eddy simulation model. *Master Thesis Delft University of Technology.*

Lesieur, M., O. Métais, and P. Comte, 2005: *Large-Eddy Simulations of Turbulence.* Cambridge University Press.

Liu, Z., Y. Hu, and W. Wang, 2019: Large eddy simulations of the flow fields over simplified hills with different roughness conditions, slopes, and hill shapes: A systematical study. *Energies*, **12**.

Lopes, A., J. Palma, and F. Castro, 2007: Simulation of the Askervein flow. Part 2: Large-Eddy Simulations. *Boundary-Layer Meteorology*, **125**, 85–108.

Mason, P., 1989: Large-eddy simulation of the convective atmospheric boundary layer. *Journal of the Atmospheric Sciences*, **46**, 1492–1516.

Panosetti, D., S. Böing, L. Schlemmer, and J. Schmidli, 2016: Idealized large-eddy and convection-resolving simulations of moist convection over mountainous terrain. *Journal of the Atmospheric Sciences*, **73**, 4021–4041.

Piomelli, U. and E. Balaras, 2002: Wall-layer models for large-eddy simulations. *Annual Review of Fluid Mechanics*, **34**, 349–374.

Pourquie, M., W. Breugen, and B. Boersma, 2009: Some issues related to the use of immersed boundary methods to represent square obstacles. *International Journal for Multiscale Computational Engineering*, **7**, 509–522.

Reynolds, O., 1895: IV on the dynamical theory of incompressible viscous fluids and the determination of the criterion. *Philosophical transactions of the royal society of london*, **186**, 123–164.

Stull, R., 1988: *An introduction to boundary layer meteorology.* Kluwer Academic Publishers, Dordrecht, the Netherlands.

Sullivan, P. P. and E. G. Patton, 2011: The effect of mesh resolution on convective boundary layer statistics and structures generated by large-eddy simulation. *Journal of the Atmospheric Sciences*, **68 (10)**, 2395–2415.

Taylor, P. A. and H. W. Teunissen, 1987: The Askervein Hill project: Overview and background data. *Boundary-Layer Meteorology*, **39**, 15–39.

Tomas, J., 2016: Obstacle-resolving large-eddy simulation of dispersion in urban environments: Effects of stability and roughness geometry. *Doctoral thesis, Delft University of Technology.*

Travin, A., M. Shur, P. Spalart, and M. Strelets, 2004: On urans solutions with LES-like behaviour. *European Congress on Computational Methods in Applied Sciences and Engineering,* **(October 2014)**.

van Dorp, P., 2016: Large-eddy simulation of wind farms in clear and cloud-topped boundary layers. *Master's thesis, Delft University of Technology, the Netherlands.*

Wyngaard, J., 2004: Toward numerical modeling in the "terra incognita". *Journal of the Atmospheric Sciences,* **61**, 1816–1826.

Wyngaard, J., 2010: *Turbulence in the Atmosphere.* Cambridge University Press.

Appendix

Filtering

Any variable ϕ will be split in a resolved part $\widetilde{\phi}$ and a subgrid part ϕ' for scales smaller than the gridsize. For LES to properly function, it is necessary that $\frac{\phi'}{\phi} << 1$. $\widetilde{\phi}$ is also an operator on ϕ, averaging over the gridbox. Its use is described in (Reynolds 1895). For the incompressibility equation, using the operator leads to

$$\frac{\partial \widetilde{u_i}}{\partial x_i} = 0. \tag{38}$$

Any ϕ can be split according to

$$\phi = \widetilde{\phi} + \phi' \tag{39}$$

and the momentum formula 2 can thus be rewritten to

$$\frac{\partial(\widetilde{u_i} + u_i')}{\partial t} + \frac{\partial(\widetilde{u_i u_j} + \widetilde{u_i} u_j' + \widetilde{u_j} u_i' + u_i' u_j')}{\partial x_j} = -\frac{1}{\widetilde{\rho} + \rho'}\frac{\partial(\widetilde{p} + p')}{\partial x_i} - g\delta_{i3} + 2f_{\epsilon ij3}(\widetilde{u_j} + u_j')\partial_k. \tag{40}$$

Since ϕ' are subgrid contributions, the mean of ϕ' over a gridbox will be zero $\widetilde{\phi'} = 0$. Calculating the mean of ϕ over any gridbox loses the singular ϕ' contributions. First, the pressure term in equation 40 has to be modified to average this term.

$$\frac{1}{\widetilde{\rho} + \rho'}\frac{\partial(\widetilde{p} + p')}{\partial x_i} \approx \frac{1}{\widetilde{\rho}}(1 - \frac{\rho'}{\widetilde{\rho}})\frac{\partial(\widetilde{p} + p')}{\partial x_i} \approx \frac{1}{\widetilde{\rho}}\frac{\partial(\widetilde{p} + p')}{\partial x_i} - \frac{\rho'}{\widetilde{\rho}}\frac{\partial\widetilde{p}}{\partial x_i} \tag{41}$$

Averaging equation 40 then leads to

$$\frac{\partial \widetilde{u_i}}{\partial t} + \frac{\partial(\widetilde{u_i u_j} + \widetilde{u_i' u_j'})}{\partial x_j} = -\frac{1}{\widetilde{\rho}}\frac{\partial\widetilde{p}}{\partial x_i} - g\delta_{i3} + \epsilon_{ij}\widetilde{u_j}f \tag{42}$$

$\widetilde{u_i' u_j'} << \widetilde{u_i u_j}$. (p_0, ρ_0, θ_0) will be a reference state, the background (p, ρ, θ).

$$\frac{\partial p_0}{\partial x_3} = -\rho_0 g \tag{43}$$

is the hydrostatic balance. $p_\infty = p_0 + \rho_0 g z$ is called the large scale pressure. The Boussinesq approximation will be used, along the notion that no water content is used in this paper, and this states that $\tilde{\rho} \approx \rho_0$ if g is adjusted to $g\left(1 - \frac{\tilde{\theta} - \theta_0}{\theta_0}\right)$ (Stull 1988).

$$\frac{\partial \widetilde{u_i}}{\partial t} + \frac{\partial(\widetilde{u_i u_j})}{\partial x_j} = -\frac{1}{\rho_0}\frac{\partial(\widetilde{p} - p_0 + p_\infty)}{\partial x_i} + g\frac{\widetilde{\theta} - \theta_0}{\theta_0}\delta_{i3} + \epsilon_{ij3}\widetilde{u_j}f. \tag{44}$$

Along with the adjustment towards τ

$$\tau_{ij} = \widetilde{u_i u_j} - \widetilde{u_i}\widetilde{u_j} - \frac{2}{3}\delta_{ij}\tilde{e} \tag{45}$$

where $\tilde{e} = (\widetilde{u_i u_i} - \widetilde{u}_i \widetilde{u}_i)/2$ is the subgrid kinetic energy, which will prove to be handy later, does the equation become

$$\frac{\partial \widetilde{u}_i}{\partial t} + \frac{\partial (\widetilde{u}_i \widetilde{u}_j)}{\partial x_j} = -\frac{1}{\rho_0} \frac{\partial p_\infty}{\partial x_i} - \frac{\partial \widetilde{\pi}}{\partial x_i} + g \frac{\widetilde{\theta} - \theta_0}{\theta_0} \delta_{i3} - \frac{\partial \tau_{ij}}{\partial x_j} + \epsilon_{ij3} \widetilde{u}_j f \qquad (46)$$

where $\pi = \frac{\widetilde{p} - p_0}{\rho_0} + \frac{2}{3} \widetilde{e_{\text{sgs}}}$ is the modified pressure, θ the potential temperature.

Runs 10 and 15
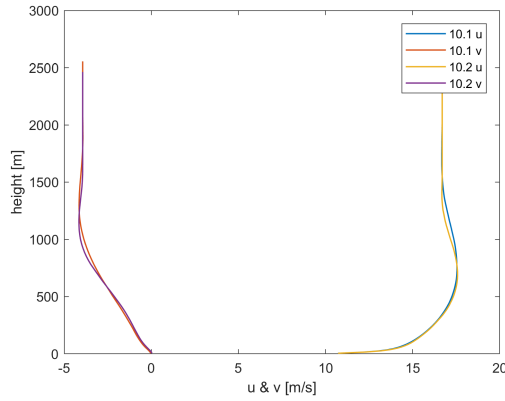
Figure 19: The velocity profiles of runs 10.1 and 10.2.
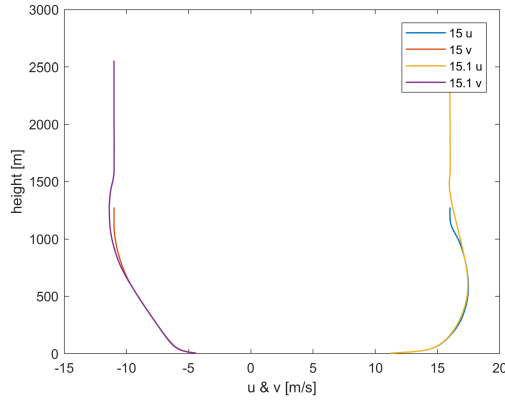
Figure 20: The velocity profiles of runs 15 and 15.1.

Adjusted DALES code

- The subgrid TKE is added to the fielddump output.

- The extra up(i,j,1) and vp(i,j,1) calculation in modibm is removed.

- The correction from $bc_{height} + 1$ to ksfc in modsurface

- The use of $dzf(ksfc)$ instead of $zf(ksfc)$ in the calculation of C_m in modsurface.

- Double /dx removed in modibm in tempwp calculation.

- With the use of $simid = Netid$ is established that the applyIBM routine doesn't function for the reference run.

- nudgeboundary is placed later in the program module.

- The run will be aborted when IBM is used without lmostlocal.

- Nair, libm and Nwall were wrongfully deallocated.

- dthvdz is translated to $(i, j, ksfc)$.

- wp is also set such that w is zero at $lnorm_z$ in modibm.

- A missing ρ was added in advecc2nd

- The second Obukhov loop is no longer fatal when lmostlocal is on.

Immersed Boundaries
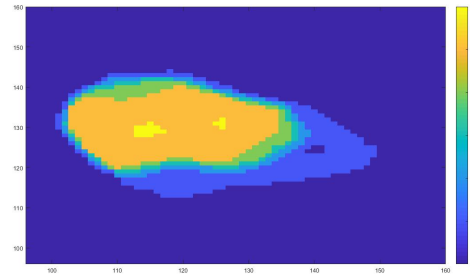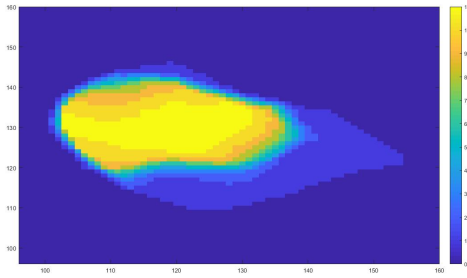
(a) Immersed Boundary for run A with $\Delta x = 4$, $\Delta z = 1$.

(b) Immersed Boundary for run B with $\Delta x = 4$, $\Delta z = 2$.
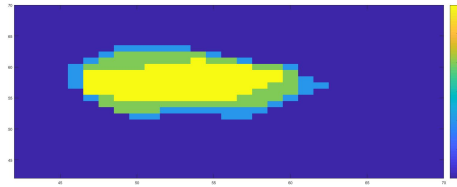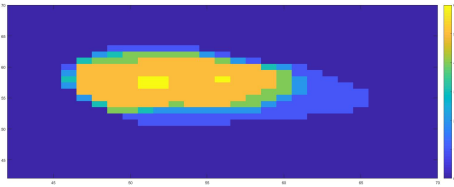
(c) Immersed Boundary for run C with $\Delta x = 10$, $\Delta z = 2$.

(d) Immersed Boundary for run D with $\Delta x = 10$, $\Delta z = 4$.
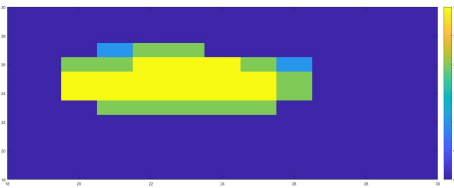
(e) Immersed Boundary for run E with $\Delta z = 25$, $\Delta z = 4$.

Figure 21: The immersed boundaries as used for runs A-E.